Journal of Statistical Physics, Vol. 110, Nos. 3–6, March 2003 (© 2003)

Ising Field Theory in a Magnetic Field: Analytic Properties of the Free Energy

P. Fonseca[1] **and A. Zamolodchikov**[1]

Received March 5, 2002

We study the analytic properties of the scaling function associated with the $2D$ Ising model free energy in the critical domain $T \to T_c$, $H \to 0$. The analysis is based on numerical data obtained through the Truncated Free Fermion Space Approach. We determine the discontinuities across the Yang–Lee and Langer branch cuts. We confirm the standard analyticity assumptions and propose "extended analyticity;" roughly speaking, the latter states that the Yang–Lee branching point is the nearest singularity under Langer's branch cut. We support the extended analyticity by evaluating numerically the associated "extended dispersion relation."

KEY WORDS: Ising model; free energy; analytic structure; metastability.

1. INTRODUCTION

The $2D$ Ising model is one of the best studied systems in statistical mechanics. Nonetheless, some questions concerning its criticality, notably in the presence of an external field H, remain open. The Ising model free energy exhibits a singularity at the critical point $H = 0$, $T = T_c$. The singularity is described in terms of the Euclidean quantum field theory known as the Ising Field Theory (IFT). It can be defined as a perturbed conformal field theory through the action

$$\mathscr{A}_{\text{IFT}} = \mathscr{A}_{(c=1/2)} + \tau \int \epsilon(x)\, d^2x + h \int \sigma(x)\, d^2x, \tag{1.1}$$

---

[1] Department of Physics and Astronomy, Rutgers University, Piscataway, New Jersey 08855-0849; e-mail: pfonseca@physics.rutgers.edu

0022-4715/03/0300-0527/0

where $\mathscr{A}_{(c=1/2)}$ stands for the action of $c=1/2$ conformal field theory (CFT) of free massless Majorana fermions, $\sigma(x)$ and $\epsilon(x)$ are primary fields of conformal dimensions $1/16$ and $1/2$. To be precise, we assume that the normalizations of these fields are fixed by the usual CFT convention,

$$|x|^2 \langle \epsilon(x)\, \epsilon(0)\rangle \to 1; \qquad |x|^{1/4} \langle \sigma(x)\, \sigma(0)\rangle \to 1 \qquad \text{as} \quad |x| \to 0. \tag{1.2}$$

Under this normalization, the parameters τ and h in (1.1) have mass dimensions 1 and 15/8, respectively. These parameters represent a deviation from the Ising model critical point,

$$\tau = C_\tau\, \varDelta T(1+O(\varDelta T, H^2)), \tag{1.3a}$$

$$h = C_h H(1+O(\varDelta T, H^2)), \tag{1.3b}$$

where $\varDelta T = 1 - T/T_c$, and real positive constants C_τ, C_h (as well as the higher-order terms in the above relations) depend on the details of the microscopic (lattice) interaction.[2] The leading singular part $\mathscr{F}_{\text{sing}}(T, H)$ of the Ising model specific free energy is universal, and it coincides with the vacuum energy density of the IFT (1.1); in what follows we use the notation $F(2\pi\tau, h)$ for this quantity. It can be expressed through a universal scaling function $\varPhi(\eta)$ of a single variable—the scaling parameter

$$\eta = 2\pi\tau / h^{8/15} \tag{1.4}$$

(see Eq. (3.20) later for the precise definition of $\varPhi(\eta)$). This scaling function is of much interest as it controls all thermodynamic properties of the Ising model in the critical domain. Although there are many exact results (obtained through exact solutions of (1.1) at $h=0$ and all τ,(4–8) and at $\tau=0$ and all h;(9, 10) these data are collected in ref. 11) as well as much numerical data(1, 12–15) about this function, its complete analytic characterization is still lacking.

In this work we report preliminary results of a numerical study of the analytic properties of this scaling function. We use certain modification of the well-known Truncated Conformal Space Approach (TCSA),(16, 17) which we call Truncated Free-Fermion Space Approach (TFFSA). Although this modification is designed specificaly to treat the case of IFT (while TCSA is applicable to a wide class of perturbed CFT), in our case it produces better accuracy by taking full advantage of the fact that at $h=0$ the IFT (1.1) is a

---

[2] For the Ising models with nearest-neighbour interactions on square and triangular lattices, specific values of these constants can be found in refs. 1 and 2; for higher order terms in Eqs. (1.3) see refs. 3 and 2.

free-fermion theory.(4, 5) Using this approach, we compute numerically the scaling function $\Phi(\eta)$ for real as well as for some complex values of η, to the accuracy sufficient to make exploration of its analytic structure in the complex η-plane. We locate the Yang–Lee edge singularity,(18, 19) and estimate some of its characteristics. Also, we study the free energy $F(2\pi\tau, h)$ at real $\tau > 0$ (low-temperature regime) and complex h; in particular, we determine, with reasonable accuracy, the imaginary part of the metastable branch of F for small as well as large values of h. For small h our result is in good agreement with the prediction from the critical droplet calculations;(20, 21) moreover, we find a leading correction to the droplet model asymptotic. We formulate an "extended analyticity conjecture" which states, roughly speaking, that the continuation of the free energy under Langer's branch cut is analytic all the way down to the Yang–Lee singularity. We then use our numerical data to support this conjecture by verifying the associated "extended dispersion relation."

The paper is arranged as follows: In Section 2 some details of the TFFSA are presented. In Section 3 we discuss what is known and what is expected on the analytic properties of the free energy in the critical domain. Basic notations used throughout the paper are introduced there. The extended analyticity conjecture is formulated in Section 4, where the associated dispersion relation is also derived. In Section 5 we briefly discuss the excited ("meson") states of IFT, and the role of the "false vacuum" resonance in the formation of the finite-size energy spectrum in this theory. The relation between the width of this resonance and the separation between the meson energy levels at the "near-intersection" points is presented there. Qualitative pictures of finite-size energy levels for real and pure imaginary h obtained through the TFFSA are described in Section 6, where we also explain in some detail how accurate numerical data for the scaling function are extracted from the finite-size spectra. The data is described in Section 7, and in Section 8 we present our analytical interpretation of it. That includes approximations of the discontinuities across the Yang–Lee and Langer branch cuts, and numerical evaluation of the corresponding dispersion relations. Numerical support for the extended analyticity is also presented in this section. In Section 9 we discuss possible physical significance of the extended analyticity.

2. THE TRUNCATED FREE-FERMION SPACE APPROACH

As is well known (see, e.g., ref. 22), at zero external field the Ising model is equivalent to a free-fermion theory. Correspondingly, (1.1) can be written as

$$\mathscr{A}_{\mathrm{IFT}} = \mathscr{A}_{\mathrm{FF}} + h \int \sigma(x)\, d^2x, \tag{2.1}$$

$$\mathscr{A}_{\mathrm{FF}} = \frac{1}{2\pi} \int [\psi \bar{\partial} \psi + \bar{\psi} \partial \bar{\psi} + im\, \bar{\psi} \psi]\, d^2x, \qquad m = 2\pi\tau. \tag{2.2}$$

Here $\partial = \frac{1}{2}(\partial_{\mathrm{x}} - i\partial_{\mathrm{y}})$, $\bar{\partial} = \frac{1}{2}(\partial_{\mathrm{x}} + i\partial_{\mathrm{y}})$, where $x = (\mathrm{x}, \mathrm{y})$ are Cartesian coordinates, ψ, $\bar{\psi}$ are chiral components of the Majorana fermi field, and $\sigma(x)$ is the "spin field" associated with this fermion.

As in standard TCSA (see, e.g., ref. 23 and references therein), we start with the IFT (1.1) in finite-size geometry, with one of the two Euclidean coordinates compactified on a circle of circumference R, $\mathrm{x} + R \sim \mathrm{x}$. If y is treated as (Euclidean) time, the finite-size Hamiltonian associated with (2.1) can be written as

$$H_{\mathrm{IFT}} = H_{\mathrm{FF}} + hV, \qquad V = \int_0^R \sigma(\mathrm{x})\, d\mathrm{x}, \tag{2.3}$$

where H_{FF} is the Hamiltonian of the free-fermion theory (2.2). We are interested in the eigenvalues of H_{IFT}, particularly in its ground-state energy $E_0(R, m, h)$, because for large R one expects to have

$$E_0(R, m, h) = RF(m, h) + O(\exp(-M_1 R)), \tag{2.4}$$

with M_1 being the gap in the spectrum of H_{IFT} at $R = \infty$, i.e., the mass of the lightest particle of the field theory (1.1). In what follows, in refering to the eigenvalues of the Hamiltonian (2.3) we typically use the notation $E(R)$, with the arguments m, h suppressed; in particular, $E_0(R)$ will stand for the ground-state eigenvalue of (2.3).

The free part H_{FF} of the Hamiltonian (2.3) is diagonal in the basis of N-particle states of free fermions of mass $|m|$. At finite R the space of states of (2.2) splits into two sectors, the Neveu–Schwartz (NS) sector and Ramond (R) sector (with $\psi, \bar{\psi}$ antiperiodic or periodic as $\mathrm{x} \to \mathrm{x} + R$, respectively). In each sector the particle momenta are quantized as $p_n = 2\pi n / R$ where $n \in \mathbb{Z} + 1/2$ in NS sector, and $n \in \mathbb{Z}$ in R sector. In what follows we typically use the notation n_i for integers, and k_i for half-integers. The N-particle states can be obtained from the NS and R vacua $|0\rangle_{\mathrm{NS}}$ and $|0\rangle_{\mathrm{R}}$ by applying the corresponding canonical fermionic creation operators,

$$\text{NS sector:} \quad |k_1, \dots, k_N\rangle_{\mathrm{NS}} = a^\dagger_{k_1} \cdots a^\dagger_{k_N} |0\rangle_{\mathrm{NS}} \qquad k_1, \dots, k_N \in \mathbb{Z} + 1/2, \tag{2.5a}$$

$$\text{R sector:} \quad |n_1, \dots, n_N\rangle_{\mathrm{R}} = a^\dagger_{n_1} \cdots a^\dagger_{n_N} |0\rangle_{\mathrm{R}} \qquad n_1, \dots, n_N \in \mathbb{Z}. \tag{2.5b}$$

The normalizations of these states are fixed (up to phases) by conventional anticommutators,

$$\{a_k, a_{k'}^\dagger\} = \delta_{k,k'}, \qquad \{a_n, a_{n'}^\dagger\} = \delta_{n,n'}. \tag{2.6}$$

In all cases the energies associated with the N-particle states, $E_N(R)$, have standard form

$$E_{N(\mathrm{NS})}(R) = E_{0(\mathrm{NS})}(R) + \sum_{i=1}^{N} \omega_{k_i}(R), \tag{2.7a}$$

$$E_{N(\mathrm{R})}(R) = E_{0(\mathrm{R})}(R) + \sum_{i=1}^{N} \omega_{n_i}(R), \tag{2.7b}$$

where

$$\omega_k(R) = \sqrt{m^2 + (2\pi k/R)^2}; \qquad \omega_n(R) = \sqrt{m^2 + (2\pi n/R)^2} \tag{2.8}$$

(with positive branch of the square root taken, in particular, $\omega_0(R) = |m|$), and

$$E_{0(\mathrm{NS})}(R) = RF(m,0) - |m| \int_{-\infty}^{\infty} \frac{d\theta}{2\pi} \cosh\theta \log(1 + e^{-|m| R \cosh\theta}), \tag{2.9a}$$

$$E_{0(\mathrm{R})}(R) = RF(m,0) - |m| \int_{-\infty}^{\infty} \frac{d\theta}{2\pi} \cosh\theta \log(1 - e^{-|m| R \cosh\theta}), \tag{2.9b}$$

are the eigenvalues associated with $|0\rangle_{\mathrm{NS}}$ and $|0\rangle_{\mathrm{R}}$, respectively. The term

$$F(m,0) = \frac{m^2}{8\pi} \log m^2 \tag{2.10}$$

in Eqs. (2.9) accounts for the famous Onsager's singularity of the Ising free energy at zero h.$^{(4)}$

In order to treat the IFT with nonzero h we can admit only the states which respect the periodicity condition for the spin field, $\sigma(\mathrm{x}+R, \mathrm{y}) = +\sigma(\mathrm{x}, \mathrm{y})$. This condition brings a distinction between the cases $m > 0$ (the "low-T regime") and $m < 0$ (the "high-T regime"). The admissible states are

$$m > 0: \quad \text{NS-states with } N \text{ even}, \quad \text{and} \quad \text{R-states with } N \text{ even}, \tag{2.11a}$$

$$m < 0: \quad \text{NS-states with } N \text{ even}, \quad \text{and} \quad \text{R-states with } N \text{ odd}. \tag{2.11b}$$

(at $m=0$ the odd-N states in the R sector can be viewed as even-N states, with one a_0 particle added). All the above statements are well-known (see, e.g., ref. 22).

The operator hV in the full Hamiltonian (2.3) generates transitions between the states in NS and R sectors. Fortunately, all its matrix elements between the above states are known exactly. They are related in a simple way to the finite-size formfactors of the field $\sigma(x)$, for which an explicit expression exists,

$$
\begin{aligned}
&{}_{\mathrm{NS}}\langle k_1, k_2,\dots, k_K|\, \sigma(0,0)\, |n_1, n_2,\dots, n_N\rangle_{\mathrm{R}}\\
&\quad = S(R) \prod_{j=1}^{K} \tilde{g}(\theta_{k_j}) \prod_{i=1}^{N} g(\theta_{n_i})\, F_{K,N}(\theta_{k_1},\dots, \theta_{k_K} \,|\, \theta_{n_1},\dots, \theta_{n_N}),
\end{aligned}
\tag{2.12}
$$

where θ_n (θ_k) stand for the finite-size rapidities related to the integers n (half-integers k) by the equations

$$
|m|\, R \sinh\theta_k = 2\pi k, \qquad |m|\, R\sinh\theta_n = 2\pi n. \tag{2.13}
$$

In (2.12) $F_{K,N}$ is the well-known spin-field formfactor in infinite-space,[24]

$$
\begin{aligned}
&F_{K,N}(\theta_1,\dots,\theta_K \,|\, \theta'_1,\dots,\theta'_N)\\
&\quad = i^{[\frac{K+N}{2}]}\bar{\sigma} \prod_{0<i<j\leqslant K} \tanh\left(\frac{\theta_i-\theta_j}{2}\right) \prod_{0<p<q\leqslant N} \tanh\left(\frac{\theta'_p-\theta'_q}{2}\right)\\
&\qquad \times \prod_{\substack{0<s\leqslant K\\ 0<t\leqslant N}} \coth\left(\frac{\theta_s-\theta'_t}{2}\right),
\end{aligned}
\tag{2.14}
$$

where

$$
\bar{\sigma} = \bar{s}\, |m|^{1/8}, \qquad \bar{s} = 2^{1/12} e^{-1/8} A^{3/2} = 1.35783834\dots \tag{2.15}
$$

(with A standing for the Glaisher's constant), and the rest of the factors represent finite-size effects. The overall factor $S(R)$ is essentially the vacuum-vacuum matrix element

$$
\bar{\sigma} S(R) = \begin{cases} {}_{\mathrm{NS}}\langle 0|\, \sigma(0,0)\, |0\rangle_{\mathrm{R}} & \text{for} \quad m>0,\\ {}_{\mathrm{NS}}\langle 0|\, \mu(0,0)\, |0\rangle_{\mathrm{R}} & \text{for} \quad m<0, \end{cases} \tag{2.16}
$$

where $\mu(x)$ is the usual dual spin field,$^{(25)}$ and $S(R)$ is given by

$$S(R) = \exp\left\{\frac{(mR)^2}{2} \iint_{-\infty}^{\infty} \frac{d\theta_1\, d\theta_2}{(2\pi)^2} \frac{\sinh\theta_1 \sinh\theta_2}{\sinh(mR\cosh\theta_1)\sinh(mR\cosh\theta_2)} \times \log\left|\coth\frac{\theta_1-\theta_2}{2}\right|\right\}, \tag{2.17}$$

which was obtained in ref. 26. The momentum-dependent leg factors g and $\tilde{g}$ are

$$g(\theta) = e^{\kappa(\theta)}/\sqrt{|m|\, R\cosh\theta}, \qquad \tilde{g}(\theta) = e^{-\kappa(\theta)}/\sqrt{|m|\, R\cosh\theta}, \tag{2.18}$$

where

$$\kappa(\theta) = \int_{-\infty}^{\infty} \frac{d\theta'}{2\pi} \frac{1}{\cosh(\theta-\theta')} \log\left(\frac{1-e^{-|m|\, R\cosh\theta'}}{1+e^{-|m|\, R\cosh\theta'}}\right). \tag{2.19}$$

The phase factors $i^{[\frac{K+N}{2}]}$ (where $[\cdots]$ denotes the integer part of the number) appearing in (2.14) can be removed by an appropriate phase rotation of the states, and thus play no role in the TFFSA computations.

The above expression (2.12) can be extracted from the result of recent papers.$^{(27)}$ In fact, we have obtained it independently, before ref. 27 appeared, by a different approach. As our derivation seems to be simpler, we outline it in Appendix A. This expression is the $m \neq 0$ generalization of corresponding massless matrix elements used in ref. 17 in the TCSA study of IFT with $m = 0$.

It is useful to note that the Hamiltonian (2.3) can be rewritten to make its scaling form explicit,

$$H_{\text{IFT}} = E_{0(\text{NS})}(R) + |m|\, H_0(r) + |m|\, \xi H_\sigma(r), \tag{2.20}$$

where

$$\xi = h/|m|^{15/8} \tag{2.21}$$

and the operators $H_0(r)$ and $H_\sigma(r)$ (corresponding to the terms H_{FF} and hV in (2.3)) depend on a dimensionless parameter $r = |m|\, R$ only.

The bulk energy density $F(m, h)$ can be extracted from the large-R asymptotic behaviour (2.4) of the ground-state eigenvalue of (2.3). As follows from (2.20), it has the form

$$F(m, h) = \frac{m^2}{8\pi}\log m^2 + m^2 G(\xi), \tag{2.22}$$

where the first term is inherited from (2.10); the scaling function $G(\xi)$ (and related function $\Phi(\eta)$ defined in (3.20) later) is the main object of our interest in this paper.

It is hardly possible to diagonalize the Hamiltonian (2.3) exactly. To render it tractable by numerical methods we follow the idea of TCSA, i.e., we use finite-dimensional approximations ("truncations") of the infinite dimensional space of the states (2.5), which include only the states of sufficiently low energy. The truncated Hamiltonian can be diagonalized numericaly, yielding an approximation to the ground-state energy function $E_0(R)$; the free energy is then extracted from its behaviour at sufficiently large R, according to (2.4). More details about this analysis are presented in Section 6.

3. ANALYTIC PROPERTIES OF THE SCALING FUNCTION

In this section we discuss known results and expected analytic properties of the scaling function in (2.22).

In fact, to describe the free energy $F(m, h)$ for both positive and negative m one needs two scaling functions $G(\xi)$ in (2.22). Although these two functions are analytically related (see Section 3.3 later) we use separate notations $G_{\text{low}}(\xi)$ for $m > 0$ and $G_{\text{high}}(\xi)$ for $m < 0$; these functions describe the free energy in low-T and high-T regimes, respectively. Both functions are defined so that $G_{\text{low}}(0) = G_{\text{high}}(0) = 0$.

3.1. The Function $G_{\text{high}}(\xi)$

This function is even, i.e., $G_{\text{high}}(\xi) = G_{\text{high}}(-\xi)$. Around $\xi = 0$ it can be represented by a convergent power series in ξ^2,

$$G_{\text{high}}(\xi) = G_2\xi^2 + G_4\xi^4 + G_6\xi^6 + \cdots. \tag{3.1}$$

This series coincides with the perturbative expansion in h in the field theory (1.1). The first coefficient G_2 is known through this perturbation theory exactly,(7) and the coefficient G_4 was obtained with high accuracy by using formfactor expansion of the four-spin correlation function.(28) There is a substantial amount of numerical data on the further coefficients. What appears to be rather accurate estimates of G_{2k} up to G_{12} are presented in a recent paper.(15) The data on these coefficients are collected in Table I.

The function $G_{\text{high}}(\xi)$ can be analyticaly continued to complex values of ξ. The Yang–Lee theory(18, 19) guarantees analyticity of $G_{\text{high}}(\xi)$ in the whole complex ξ plane with possible exception of the imaginary axis. At

Table I. Numerical Values of the Coefficients G_{2n} in (3.1). The First Column Contains the Data from Refs. 7 and 15. The Results Obtained Through High-T Dispersion Relation, Eq. (3.5), with the Use of Our Approximation (8.2), Are Presented in the Second Column

	From References	From high-T dispersion relation
G_2	$-1.8452280\ldots$ (7)	-1.8452283
G_4	$8.33370(1)$ (15)	8.33410
G_6	$-95.1689(4)$ (15)	-95.1884
G_8	$1457.55(11)$ (15)	1458.21
G_{10}	$-25884(13)$ (15)	-25889
G_{12}	$5.03(1)\times 10^5$ (15)	5.02×10^5
G_{14}	—	-1.04×10^7

the imaginary axis one expects to observe branch cuts resulting from condensation of the Yang–Lee zeroes of the partition function in the thermodynamic limit. These branch cuts extend from $i\xi_0$ to $i\infty$ and from $-i\xi_0$ to $-i\infty$, as shown in Fig. 1, where ξ_0 is some positive constant whose numerical value will be estimated in the Section 6,

$$\xi_0 = 0.18930(5). \tag{3.2}$$

The branching points $\pm i\xi_0$ represent the Yang–Lee edge singularity.(18) Combining these analytic properties with the asymptotic behaviour $G_{\text{high}}(\xi) \simeq \xi^{16/15}$ (see Eq. (3.34) later) one can derive the dispersion relation(19)

$$G_{\text{high}}(\xi) = -\xi^2 \int_{\xi_0}^{\infty} \frac{2\,\Im m\, G_{\text{imh}}(t)}{t(t^2+\xi^2)} \frac{dt}{\pi}, \tag{3.3}$$

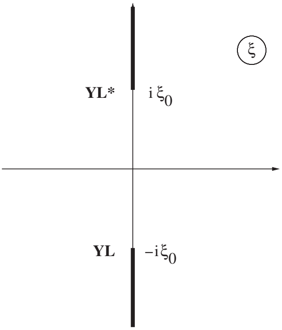

Fig. 1. Analytic structure of $G_{\text{high}}(\xi)$ in the complex ξ plane. YL and YL* denote the Yang–Lee edge singularities; associated branch cuts are shown as solid lines.

where the imaginary part of the function

$$G_{\text{imh}}(t) \equiv G_{\text{high}}(-it+0) \tag{3.4}$$

relates in the usual way to the discontinuity across either of the branch cuts in Fig. 1. In particular, the coefficients G_{2n} in (3.1) can be expressed in terms of this function as

$$G_{2n} = (-)^n \int_{\xi_0}^{\infty} \frac{2\,\Im m\, G_{\text{imh}}(t)}{t^{2n+1}} \frac{dt}{\pi}. \tag{3.5}$$

In what follows we will refer to (3.3) as the high-T dispersion relation.

As is known,$^{(29)}$ the Yang–Lee edge singularity is a critical point, and the associated CFT was identified in ref. 30 as the (nonunitary) minimal model with central charge $c_{\text{YL}} = -22/5$. This CFT has only one relevant operator, the primary field of conformal dimension $\Delta_{\text{YL}} = -1/5$. Therefore, one expects the singularities of $G_{\text{high}}(\xi)$ at $\xi = \pm i\xi_0$ to be of the form

$$G_{\text{high}}(\xi) = \mathcal{G}_A(\xi) + (\xi_0^2+\xi^2)^{\frac{5}{6}}\,\mathcal{G}_B(\xi) + (\xi_0^2+\xi^2)^{\frac{5}{3}}\,\mathcal{G}_C(\xi)$$
$$+\,\text{subleading singular terms}, \tag{3.6}$$

where the functions $\mathcal{G}_A(\xi), \mathcal{G}_B(\xi), \mathcal{G}_C(\xi),\ldots,$ are regular at $\xi = \pm i\xi_0$. To some degree, the singular terms in (3.6) can be understood in terms of the low-energy *effective* action

$$\mathcal{A}_{\text{eff}} = \mathcal{A}_{\text{LYCFT}} + i\,|m|^{\frac{12}{5}}\,\lambda(\xi) \int \phi_{-1/5}(x)\, d^2x + \frac{\alpha(\xi)}{(2\pi m)^2} \int (T\bar{T})(x)\, d^2x$$
$$+\,\text{higher irrelevant operators}, \tag{3.7}$$

where $\phi_{-1/5}$ is the relevant primary field mentioned above, and the rest of the action contains the contributions of irrelevant operators, the field $(T\bar{T})$ (i.e., the $L_{-2}\bar{L}_{-2}$ descendent of the identity operator) being the lowest of such operators. The dimensionless coupling constants $\lambda(\xi), \alpha(\xi),\ldots,$ are certain functions of the scaling parameter ξ, universal in the sense that they are uniquely determined by the original field theory (1.1) (but taken as "input" data in the effective theory (3.7)); all these functions are expected to be regular at $\xi = \pm i\xi_0$, and the critical point(s) $\pm i\xi_0$ is defined by the condition $\lambda(\pm i\xi_0) = 0$. Thus, in the vicinity of, say, $-i\xi_0$

$$\lambda(\xi) = \lambda_1(\xi_0^2+\xi^2) + O((\xi_0^2+\xi^2)^2); \tag{3.8a}$$

$$\alpha(\xi) = \alpha_0 + O(\xi_0^2+\xi^2); \tag{3.8b}$$

and similarly for the other couplings.

At $\xi = -i\xi_0$ (as well as at $\xi = i\xi_0$) the field theory (1.1) describes the Renormalization Group flow from the Ising model fixed point with $c = 1/2$ down to the Yang–Lee fixed point with $c_{\mathrm{YL}} = -22/5$. In this case the mass gap M_1 vanishes, and the finite-size energy levels are expected to approach the linear asymptotic (2.4) with a power-like, not exponential, accuracy. These power-like corrections to the linear asymptotic (2.4) can be analysed through the perturbation theory based on the effective action (3.7). In particular, for the ground-state level of (2.20) with $\xi = \pm i\xi_0$ one obtains

$$E_0(R) = F_0 R + \frac{\pi}{6R}\left(-c_{\mathrm{eff}} + \frac{\pi c_{\mathrm{eff}}^2 \alpha_0}{24(mR)^2} - \frac{2\pi^2 c_{\mathrm{eff}}^3 \alpha_0^2}{(24)^2\,(mR)^4} + O(R^{-\frac{28}{5}}) \right), \tag{3.9}$$

where $c_{\mathrm{eff}} = c_{\mathrm{YL}} - 24\Delta_{\mathrm{YL}} = 2/5$ is the "effective central charge" of the Yang–Lee CFT, α_0 is the leading coefficient in (3.8b), and F_0 stands for the free energy F_0 associated with this flow; the last quantity is related to the value of the scaling function $G_{\mathrm{high}}(\xi)$ at the singular point,

$$F_0 = F(m, 0) + m^2 G_{\mathrm{high}}(\pm i\xi_0). \tag{3.10}$$

The calculation leading to (3.9) is similar to that presented in ref. 31; we skip it in this report.

3.2. The Function $G_{\mathrm{low}}(\xi)$

Unlike $G_{\mathrm{high}}(\xi)$ above, the analytic continuation of $G_{\mathrm{low}}(\xi)$ is not an even function of ξ. More precisely, for $m > 0$ the analytic continuation in h of the free energy (2.22) yields two different analytic functions, depending on whether one continues from positive or negative parts of the real axis. In what follows, by $G_{\mathrm{low}}(\xi)$ we always understand analytic continuation of the free energy from *positive* part of the real ξ axis. Again, according to the Yang–Lee theory, $G_{\mathrm{low}}(\xi)$ is analytic in the right half-plane $\Re e\,\xi > 0$. Langer's theory(20) (as well as earlier calculations within "droplet models"(32, 33)) predicts a weak singularity at $\xi = 0$, and it is usually assumed (see, e.g., refs. 34, 35, and 36) that $G_{\mathrm{low}}(\xi)$ is analytic in the full complex ξ-plane with the branch cut from 0 to $-\infty$, as is shown in Fig. 2. We will call this the *standard analyticity assumption*. This assumption will be confirmed by our numerical analysis in Section 7. The function $G_{\mathrm{low}}(\xi)$ admits an *asymptotic* expansion in powers of ξ,

$$G_{\mathrm{low}}(\xi) \simeq \tilde{G}_1 \xi + \tilde{G}_2 \xi^2 + \cdots. \tag{3.11}$$

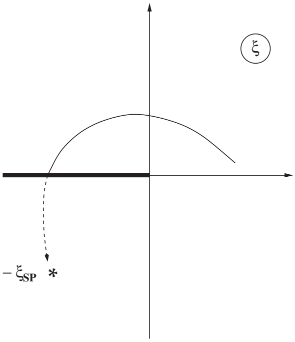

Fig. 2. Analytic structure of $G_{\mathrm{low}}(\xi)$. The solid line is the Langer's branch cut. The star denotes the nearest singularity under this branch cut; its significance is discussed in Section 9.

Again, the coefficients $\tilde{G}_n$ here in principle can be computed by means of the perturbation theory in h in (2.1). Thus, the first coefficient is directly related to the spontaneous magnetization at zero h, given by (2.15),

$$\tilde{G}_1 = -\bar{s}. \tag{3.12}$$

The coefficient $\tilde{G}_2$ is also known exactly, since its computation involves integrating the two-spin correlation function, which is determined in terms of the Painlevé functions.(7) Several further coefficients were estimated in ref. 37 using exact large-distance expansions of multi-spin correlation functions at zero h. Numerical estimates from lattice series analysis are also available.(13) We quote these results in Table II.

If one makes the above standard analyticity assumption (as in Fig. 2), the coefficients $\tilde{G}_n$ can be represented as the integrals(35)

$$\tilde{G}_n = (-)^{n+1} \int_0^\infty \frac{\Im m\, G_{\mathrm{meta}}(t)}{t^{n+1}} \frac{dt}{\pi}, \qquad n = 2, 3, 4, \ldots, \tag{3.13}$$

where the function

$$G_{\mathrm{meta}}(\xi) \equiv G_{\mathrm{low}}(-\xi + i0) \tag{3.14}$$

at positive ξ describes the values of $G_{\mathrm{low}}(\xi)$ at real negative ξ, at the upper edge of the branch cut in Fig. 2. Correspondingly, the discontinuity of $G_{\mathrm{low}}(\xi)$ across this branch cut equals $2i\, \Im m\, G_{\mathrm{meta}}(-\xi)$. The Eq. (3.13) follows directly from the dispersion relation(34, 35)

$$G_{\mathrm{low}}(\xi) = \tilde{G}_1 \xi - \xi^2 \int_0^\infty \frac{\Im m\, G_{\mathrm{meta}}(t)}{t^2\,(t+\xi)} \frac{dt}{\pi}, \tag{3.15}$$

Table II. Numerical Values of the Coefficients $\tilde{G}_n$ in (3.11). Exact Results for $\tilde{G}_1$ and $\tilde{G}_2$, and Numerical Estimates Found in Literature, Are Collected in the First Column. The Second Column Shows Results Obtained Through Low-T Dispersion Relation, Eq. (3.13), Using Our Approximation (8.14)

	From References	From high-T dispersion relation
$\tilde{G}_1$	$-1.35783834\ldots$ (22)	-1.35783835
$\tilde{G}_2$	$-0.0489532\ldots$ (7)	-0.0489589
$\tilde{G}_3$	0.0387529 (37); $0.039(1)$ (13)	0.0388954
$\tilde{G}_4$	-0.0685535 (37); $-0.0685(2)$ (13)	-0.0685060
$\tilde{G}_5$	—	0.18453
$\tilde{G}_6$	—	-0.66215
$\tilde{G}_7$	—	2.952
$\tilde{G}_8$	—	-15.69
$\tilde{G}_9$	—	96.76
$\tilde{G}_{10}$	—	-6.79×10^2
$\tilde{G}_{11}$	—	5.34×10^3
$\tilde{G}_{12}$	—	-4.66×10^4
$\tilde{G}_{13}$	—	4.46×10^5
$\tilde{G}_{14}$	—	-4.66×10^6

where the integral converges at any finite ξ because $G_{\text{low}}(\xi)\sim\xi^{16/15}$ as $\xi\to\infty$ (as follows from (3.28) and (3.29) later).

The function $G_{\text{meta}}(\xi)$ deservingly attracts much attention, for at least two reasons. One is the commonly accepted interpretation of the function

$$F_{\text{meta}}(m,h)=m^2\left(\frac{1}{8\pi}\log m^2+G_{\text{meta}}(\xi)\right),\qquad \xi=h/|m|^{15/8},\tag{3.16}$$

which coincides with the analytic continuation of the free energy (2.22) to negative values of h, as the free energy associated with the metastable state at $T<T_c$. In fact, to the best of our knowledge, it is the only mathematically precise definition of the metastable free energy available today. The function (3.16) takes complex values, and its imaginary part

$$\Gamma(m,h)\equiv\Im m\, F_{\text{meta}}(m,h)=m^2\,\Im m\, G_{\text{meta}}(\xi)\tag{3.17}$$

is interpreted as the rate of decay of the metastable state. More precisely, according to Langer's theory,(20, 38) the actual rate of decay is asymptotically proportional (with the constant factor absorbing the time scale) to this imaginary part in the limit $h\to 0$ (or $\xi\to 0$). It is tempting to assume (as is often done in the literature on nucleation theory) that similar relation extends to some finite domain of h, although it is understood that the proportionality coefficient, being sensitive to at least some details of the kinetic model, may very well depend on h, and its degree of universality is not clear. Another, and much better understood, interpretation of (3.16) is in terms of the quantum field theory (1.1) in $1+1$ Minkowski space-time. Namely, at $\tau > 0$ and $h \neq 0$ this field theory exhibits a global resonance state commonly refered to as the "false vacuum," and the quantity (3.16) coincides with the associated (complex) energy density; in particular, the imaginary part of (3.16) gives precisely the decay probability (per unit volume and per unit time) of this resonance state.(39–41) If h is small, both of the above interpretations allow one to justify the validity of the instanton saddle-point calculation, which in the $D=2$ case yields the following $h \to 0$ asymptotic behaviour of the imaginary part of (3.16)(21) (see refs. 20, 39, 40, 41, and 34 for such calculations in more general context),

$$\Gamma(m, h) \to \frac{\bar{\sigma} h}{2\pi} \exp\left(-\frac{\pi m^2}{2\bar{\sigma} h} \right) \qquad \text{as} \quad h \to 0, \tag{3.18}$$

where $\bar{\sigma} = \bar{s}\,|m|^{1/8}$ is the magnetization at zero h (see Eq. (2.15)). It is fair to say that there is still some controversy about whether (3.18) gives the correct numerical coefficient in the asymptotic behaviour of this imaginary part.(42) Our analysis in Section 7 is completely consistent with the coefficient in (3.18), and actually offers the leading correction to this asymptotic (see Eq. (5.9)).

3.3. The Function $\Phi(\eta)$

Although the scaling functions G_{high} and G_{low} above are defined independently, in fact they can be analytically related one to another. To do this it is useful to introduce another scaling variable,

$$\eta = m / |h|^{8/15}, \tag{3.19}$$

and rewrite the free energy (2.22) as

$$F(m, h) = \frac{m^2}{8\pi} \log m^2 + |h|^{16/15}\, \Phi(\eta). \tag{3.20}$$

Of course, the scaling function $\Phi(\eta)$ here is related to the function(s) $G(\xi)$ in (2.22), and vice versa. If both m and h are real and positive we have

$$\eta = 1/\xi^{8/15}, \tag{3.21}$$

and therefore

$$\Phi(\eta) = \eta^2 G_{\text{low}}(1/\eta^{15/8}) \qquad \text{for real} \quad \eta > 0. \tag{3.22}$$

Similarly, if $h > 0$ but $m < 0$ the variables (2.21) and (3.19) are related as

$$\eta = -1/\xi^{8/15}, \tag{3.23}$$

so that

$$\Phi(\eta) = \eta^2 G_{\mathrm{high}}(1/(-\eta)^{15/8}) \qquad \text{for real} \quad \eta < 0. \tag{3.24}$$

On the other hand, for fixed $h \neq 0$ the free energy $F(m, h)$, as function of m, is expected to be analytic at all finite real m, including the point $m = 0$, for if $h \neq 0$ the correlation length remains finite even at $m = 0$. Therefore the scaling function $\Phi(\eta)$ can be written as

$$\Phi(\eta) = -\frac{\eta^2}{8\pi} \log \eta^2 + \tilde{\Phi}(\eta), \tag{3.25}$$

where the function $\tilde{\Phi}(\eta)$ is analytic at all finite real η.

Equations (3.22) and (3.24) can be promoted to analytic relations valid for complex values of η. One notes that the variable transformation (3.23) maps the right half-plane in Fig. 1 onto the wedge $-4\pi/15 < \arg(-\eta) < 4\pi/15$; we call it the "High-T Wedge," see Fig. 3, where it is marked as the region HTW. Therefore the following analytic relation holds in this wedge,

$$\begin{aligned} &-\frac{\eta^2}{4\pi} \log(-\eta) + \tilde{\Phi}(\eta) \\ &\quad = \eta^2 G_{\mathrm{high}}(1/(-\eta)^{15/8}) \qquad \text{for} \quad -4\pi/15 < \arg(-\eta) < 4\pi/15, \end{aligned} \tag{3.26}$$

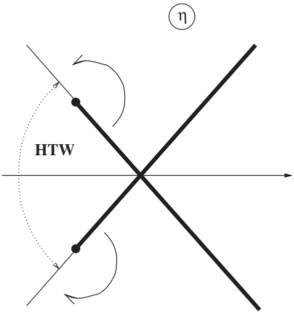

Fig. 3. Mapping of Fig. 1 under the variable transformation (3.23); the wedge HTW ($-\frac{4\pi}{15} < \arg(-\eta) < \frac{4\pi}{15}$) is the image of the right half-plane in Fig. 1. Rotating the branch cuts as suggested by the arrows opens the principal sheet of the η-plane shown in Fig. 4.

where the principle branch of the log function (i.e., $\log(y)$ is real for real $y>0$) should be taken. The Yang–Lee branching points are located at the points $\eta=-Y_0 e^{\pm i4\pi/15}$ in the complex η-plane, where

$$Y_0 = 1/\xi_0^{8/15}. \tag{3.27}$$

The way the corresponding branch cuts are drawn in Fig. 1 corresponds to placing them along the rays $\eta = y\, e^{\pm i4\pi/15}$, with y running from $-Y_0$ to $+\infty$, as is done in Fig. 3. However, it is convenient to rotate these branch cuts 180°, as is suggested by arrows in Fig. 3. This way one exposes the full "principal sheet" of the complex η plane, shown in Fig. 4, where the branch cuts extend along the rays $\eta = ye^{\pm i4\pi/15}$, $-\infty < y < -Y_0$. In this picture the way to reach the left half plane in Fig. 1 is to go from the region HTW under either of the cuts. This complication is not important, as in view of the symmetry $G_{\text{high}}(\xi) = G_{\text{high}}(-\xi)$ one expects to see there merely another copy of the principal sheet. More importantly, there is now a direct way (through some vicinity of the real axis, where $\tilde{\Phi}(\eta)$ is analytic) into the right-hand part of the principal sheet. Here, in the wedge $-4\pi/15 < \arg(\eta) < 4\pi/15$ (the domain LTW_+), which is the image of the right half plane in Fig. 2 under the variable transformation (3.21), the function $\tilde{\Phi}(\eta)$ is related to $G_{\text{low}}(\xi)$ as

$$-\frac{\eta^2}{4\pi}\log(\eta) + \tilde{\Phi}(\eta) = \eta^2 G_{\text{low}}(1/\eta^{15/8}) \qquad \text{for} \quad -4\pi/15 < \arg(\eta) < 4\pi/15, \tag{3.28}$$

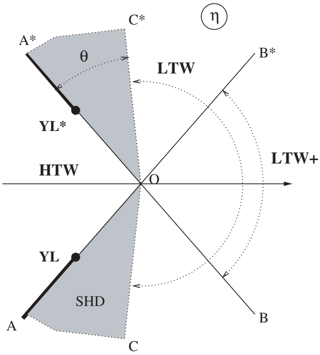

Fig. 4. Principal sheet of the η-plane for the scaling function $\tilde{\Phi}(\eta)$. The wedge LTW $(-\frac{8\pi}{15} < \arg(\eta) < \frac{8\pi}{15})$ is the image of the principal sheet in Fig. 2 under the map (3.21). Analyticity of $\tilde{\Phi}(\eta)$ in the wedge SHD $(-\frac{11\pi}{15} < \arg(\eta) < -\frac{8\pi}{15})$ is the subject of the "extended analyticity" conjecture in Section 4.

where again the principle branch of the logarithm is understood. Thus, $\tilde{\Phi}(\eta)$ is analytic in the wedges HTW and LTW_+ in Fig. 4, where it matches the functions G_{high} and G_{low} through (3.26) and (3.28), plus it is analytic in some finite neighbourhood of the point $\eta=0$. Moreover, the transformation (3.21) maps the full principal sheet of the complex ξ-plane in Fig. 2 onto twice wider "Low-T Wedge" $-8\pi/15 < \arg(\eta) < 8\pi/15$ (shown as LTW in Fig. 4), with the upper and lower edges of the branch cut in Fig. 2 represented by the rays $\arg(\eta) = \mp 8\pi/15$. The standard analyticity assumption (see Section 3.2) implies analyticity of $\tilde{\Phi}(\eta)$ in this wider wedge. Not unexpectedly, our numerical analysis in Section 8 will confirm this to an high degree of precision. The question interesting indeed is about analytic properties of this scaling function in the remaining part of the η-plane, the "Shadow Domain" $-11\pi/15 < \arg(\eta) < -8\pi/15$ (SHD in Fig. 4). Significance of this problem will be discussed in Section 9. In Section 4 later we will formulate what we believe to be the most natural conjecture about the shadow domain analyticity.

In any case, $\tilde{\Phi}(\eta)$ is analytic at $\eta = 0$, and in some finite domain around this point it can be represented as a convergent power series,

$$\tilde{\Phi}(\eta) = \Phi_0 + \Phi_1\eta + \Phi_2\eta^2 + \cdots. \tag{3.29}$$

In fact, the first two coefficients in series (3.29) are known exactly, thanks to integrability of the field theory (1.1) with $\tau = 0$.(9) The coefficient Φ_0 appears as the amplitude in its free energy,

$$F(0, h) = \Phi_0\ |h|^{16/15}, \tag{3.30}$$

which was computed in ref. 10,

$$\Phi_0 = -\frac{\Gamma(1/3)\,\Gamma(1/5)\,\Gamma(7/15)}{2\pi\Gamma(2/3)\,\Gamma(4/5)\,\Gamma(8/15)}\left(\frac{4\pi^2\Gamma^2(13/16)\,\Gamma(3/4)}{\Gamma^2(3/16)\,\Gamma(1/4)}\right)^{8/15}. \tag{3.31}$$

The coefficient Φ_1 is related to the expectation value of the energy density field $\epsilon(x)$ in this integrable theory,

$$\langle\epsilon\rangle|_{\tau=0} = -2\pi\Phi_1\ |h|^{8/15}, \tag{3.32}$$

which was determined in ref. 43,

$$\langle\epsilon\rangle|_{\tau=0} = (2.00314\ldots)\ |h|^{8/15}. \tag{3.33}$$

Table III. First Few Coefficients of the Power Series (3.29): Exact Results from Integrable Field Theory (First Column), Estimates from TFFSA Data (Second Column), and Results Obtained from the Extended Dispersion Relation, Eq. (4.10), Using Approximation (8.21) (Third Column)

	From References	From TFFSA data	From high-T dispersion relation
Φ_0	$-1.1977334...$ (10)	-1.1977331	-1.1977320
Φ_1	$-0.3188096...$ (43)	-0.3188103	-0.3188192
Φ_2	—	0.1108867	0.1108915
Φ_3	—	0.0164266	0.0164252
Φ_4	—	-2.64×10^{-4}	-2.64×10^{-4}
Φ_5	—	-5.14×10^{-4}	-5.14×10^{-4}
Φ_6	—	2.07×10^{-4}	2.09×10^{-4}
Φ_7	—	-4.52×10^{-5}	-4.48×10^{-5}
Φ_8	—	—	3.16×10^{-7}
Φ_9	—	—	4.31×10^{-6}
Φ_{10}	—	—	-1.99×10^{-6}

Further coefficients can in principle be computed using perturbation theory in τ; this however is a hard problem because multipoint correlation functions of the $\tau = 0$ theory are not known exactly (see, however, ref. 44). Our numerical analysis in Section 6 yields next six coefficients Φ_2 to Φ_7 with reasonable accuracy (see Table III).

According to (3.26) and (3.28), the coefficients Φ_n control the asymptotics of the functions $G_{\text{high}}(\xi)$ and $G_{\text{low}}(\xi)$ at large ξ; for instance, for $-\pi/2 < \arg(\xi) < \pi/2$ and sufficiently large $|\xi|$

$$G_{\text{high}}(\xi) = \Phi_0 \xi^{\frac{16}{15}} - \Phi_1 \xi^{\frac{8}{15}} + \frac{1}{15\pi} \log \xi^2 + \sum_{n=2}^{\infty} (-)^n \Phi_n \xi^{\frac{8(2-n)}{15}} \qquad \text{as} \quad \xi \to \infty. \tag{3.34}$$

Similar expansion (without the $(-)^n$ factors) holds for $G_{\text{low}}(\xi)$ in the wider domain $-\pi < \arg(\xi) < \pi$. Conversely, expansions (3.1) and (3.11) can be rewritten as large-η expansions of the scaling function $\Phi(\eta)$ in the corresponding domains of the η plane. Thus, the expansion

$$-\frac{\eta^2}{4\pi} \log(-\eta) + \tilde{\Phi}(\eta) = G_2(-\eta)^{-\frac{7}{4}} + G_4(-\eta)^{-\frac{22}{4}} + G_6(-\eta)^{-\frac{37}{4}} + \cdots$$

$$\text{for} \quad -\frac{4\pi}{15} < \arg(-\eta) < \frac{4\pi}{15} \tag{3.35}$$

converges to $\Phi(\eta)$ for sufficiently large η in the domain HTW in Fig. 4. In the domain LTW the function $\Phi(\eta)$ has asymptotic expansion

$$-\frac{\eta^2}{4\pi}\log(\eta)+\tilde{\Phi}(\eta)\simeq \tilde{G}_1\eta^{\frac{1}{8}}+\tilde{G}_2\eta^{-\frac{7}{4}}+\tilde{G}_3\eta^{-\frac{29}{8}}+\cdots \qquad \text{as} \quad \eta\to\infty,$$

$$\text{for} \quad -\frac{8\pi}{15}<\arg(\eta)<\frac{8\pi}{15}. \tag{3.36}$$

To prepare notations for our analysis in Sections 6 and 7 let us briefly describe the expected behaviour of the scaling function $\Phi(\eta)$ along the axes AOB*, A*OB and on the rays OC, OC* in Fig. 4; these domains are of particular interest for our discussion.

The axis AOB* corresponds to $\eta=e^{\frac{4\pi}{15}i}y$ with real (positive as well as negative) y. The values of the scaling function $\Phi(\eta)$ along this axis are related to the free energy $F(m,h)$ at pure imaginary h as follows. Let us introduce the function

$$\Phi_{\text{imh}}(y)=-\frac{y^2}{4\pi}\log|y|-\frac{i\,y^2}{15}+e^{-\frac{8\pi}{15}i}\tilde{\Phi}(ye^{\frac{4\pi}{15}i-i0}). \tag{3.37}$$

According to (2.22), (3.20), and (3.25), this function relates to the analytic continuations of $G_{\text{high}}(\xi)$ and $G_{\text{low}}(\xi)$ to pure imaginary ξ. Namely,

$$\Phi_{\text{imh}}(y)=y^2G_{\text{low}}(-i/y^{15/8}+0) \qquad \text{for} \quad y>0; \tag{3.38a}$$

$$\Phi_{\text{imh}}(y)=y^2G_{\text{high}}(-i/(-y)^{15/8}+0) \qquad \text{for} \quad y<0. \tag{3.38b}$$

Therefore it takes real values for $y\leqslant -Y_0$ (the upper edge of the branch cut A-YL in Fig. 4), and becomes complex-valued for $y>-Y_0$, where its imaginary part relates to imaginary part of the function (3.4),

$$D_{\text{imh}}(y)\equiv \Im m\,\Phi_{\text{imh}}(y)=y^2\,\Im m\,G_{\text{imh}}(1/(-y)^{15/8}), \qquad \text{for} \quad y<0. \tag{3.39}$$

The structure of the singularity of $\Phi_{\text{imh}}(y)$ at $-Y_0$ can be described in terms of the expansion (3.6). As in the analysis in Sections 6–8 we use the variable η rather then ξ, let us introduce here more suitable notations. In the vicinity of $-Y_0$ we expect to have

$$\Phi_{\text{imh}}(y)=A(y)+B(y)(-Y_0-y-i0)^{\frac{5}{6}}+C(y)(-Y_0-y-i0)^{\frac{5}{3}}+\cdots, \tag{3.40}$$

where the real analytic functions $A(y)$, $B(y)$, $C(y)$,..., are regular at $y=-Y_0$, i.e., they admit the power-series expansions

$$A(y)=A_0+A_1(-Y_0-y)+A_2(-Y_0-y)^2+\cdots, \tag{3.41a}$$

$$B(y)=B_0+B_1(-Y_0-y)+\cdots, \tag{3.41b}$$

$$C(y)=C_0+\cdots, \tag{3.41c}$$

around the point $-Y_0$, with real coefficients. The structure (3.40) follows from the expected form (3.7) of the effective action in the vicinity of the critical point. The first subleading singular term written down in (3.40) is due to the term $T\bar{T}$ in (3.7). Simple perturbative analysis (which we skip in this report) allows one to relate some of the coefficients in (3.41) to the parameters in (3.8),

$$B_0=f_{\mathrm{YL}}a_{\mathrm{YL}}^2(15\lambda_1 Y_0^{-\frac{47}{20}}/4)^{5/6}, \qquad C_0=\alpha_0\, B_0^2/4Y_0^2, \tag{3.42}$$

where $f_{\mathrm{YL}}=-\sqrt{3}/12$ is the free energy amplitude of the integrable Yang–Lee field theory,(45, 31) and $a_{\mathrm{YL}}=2.6429446...$ is the corresponding amplitude in its "mass to coupling relation."(31, 47)

Let us also write down the y-series expansions of (3.39), which follow directly from (3.29). For sufficiently small $|y|$ we have

$$D_{\mathrm{imh}}(y)=\sum_{n=0}^{\infty}\bar{\Phi}_n y^n, \tag{3.43}$$

where

$$\bar{\Phi}_n=\Phi_n \sin\frac{4\pi(n-2)}{15} \qquad \text{for} \quad n\neq 2; \qquad \bar{\Phi}_2=-\frac{1}{15}. \tag{3.44}$$

The axis OC in Fig. 4 (i.e., $\eta=y\,e^{-i\frac{8\pi}{15}}$ with real $y>0$) is the image of the upper edge of the branch cut in Fig. 2. The values of $\Phi(\eta)$ along this axis are related to the complex free energy (3.16),

$$\Phi_{\mathrm{meta}}(y)\equiv-\frac{y^2}{4\pi}\log y+\frac{2iy^2}{15}+e^{i\frac{16\pi}{15}}\tilde{\Phi}(ye^{-i\frac{8\pi}{15}})=y^2G_{\mathrm{meta}}(1/y^{\frac{15}{8}}). \tag{3.45}$$

In view of (3.15) and (3.17), the imaginary part of this function plays particularly important role, so we introduce for it a separate notation

$$D_{\mathrm{meta}}(y)=\Im m\,\Phi_{\mathrm{meta}}(y)=\frac{2}{15}y^2+\frac{1}{2i}(e^{i\frac{16\pi}{15}}\tilde{\Phi}(ye^{-i\frac{8\pi}{15}})-e^{-i\frac{16\pi}{15}}\tilde{\Phi}(ye^{i\frac{8\pi}{15}})). \tag{3.46}$$

As follows from (3.45), this function enjoys a power series expansion

$$D_{\text{meta}}(y)=\sum_{n=0}^{\infty} D_n y^n, \tag{3.47}$$

with

$$D_n=\Phi_n \sin\frac{8\pi(2-n)}{15} \qquad \text{for} \quad n\neq 2; \qquad D_2=\frac{2}{15}, \tag{3.48}$$

which converges for sufficiently small y. On the other hand, $D_{\text{meta}}(y)$ decays very fast at large positive y. According to (3.18),

$$D_{\text{meta}}(y)\to\frac{\bar{s}}{2\pi}V(y), \qquad \text{as} \quad y\to+\infty, \tag{3.49}$$

where $V(y)$ stands for the function

$$V(y)=y^{\frac{1}{8}}\exp(-\pi y^{\frac{15}{8}}/2\bar{s}). \tag{3.50}$$

4. EXTENDED ANALYTICITY

In the previous Section we have described the domains of analyticity of the scaling function $\tilde{\Phi}(\eta)$ which follow from previously known results. An unexplored area lays between the High-T and Low-T Wedges in Fig. 4, the "Shadow Domain" SHD. In more conventional notations (i.e., in terms of the scaling variable ξ) this domain is located under the Langer's branch cut in Fig. 2, imediately below the negative real axis. Alternatively, it can be reached by going under either of the branch cuts in Fig. 1. We believe the problem of establishing the analytic properties of free energy in the shadow domain is an important one, and it was one of the motivations of this work. Some reasons for our interest in this problem are explained in Section 9.

The simplest conceivable possibility is that the function $\tilde{\Phi}(\eta)$ is actually analytic in the wedge $-11\pi/15<\arg(\eta)<11\pi/15$ which includes the whole of the shadow domain. It is also the most elegant possibility (to our sense of beauty, that is), because it renders the Yang–Lee point an additional significance of being the closest singularity under the Langer's branch cut in Fig. 2. We formulate it as the following

Extended Analyticity Conjecture. The scaling function $\tilde{\Phi}(\eta)$ is analytic in the whole complex η-plane with two branch cuts extending from the points YL and YL* to infinity, along the rays YL$-$A and YL*$-$A* in Fig. 4, respectively.

The extended analyticity is equivalent to certain "extended" dispersion relation, expressing this scaling function in terms of its discontinuity across the branch cuts in Fig. 4. To write it down, let us introduce the function

$$\tilde{\Delta}(y) = ie^{-i\frac{8}{15}\pi}(\tilde{\Phi}(-ye^{i\frac{4}{15}\pi-i0}) - \tilde{\Phi}(ye^{-i\frac{11}{15}\pi+i0})), \tag{4.1}$$

which is the discontinuity of $\tilde{\Phi}(\eta)$ across the branch cut YL$-$A, with additional phase factor introduced for later convenience. Here y is a positive real variable interpreted as the coordinate along the ray $O-A$ in Fig. 4. The function (4.1) vanishes for $y < Y_0$, while at $y > Y_0$ it takes complex values. In the last domain it coincides with certain analytic continuation of the function $D_{\mathrm{imh}}(y)$,

$$\tilde{\Delta}(Y_0 + z) = D_{\mathrm{imh}}(-Y_0 + z\,e^{-i\pi+i0}), \qquad (z > 0). \tag{4.2}$$

Unfortunately, this function grows too fast at large positive y ($\tilde{\Delta}(y) \to -y^2/4$ as $y \to +\infty$), and writing down the dispersion integral directly for $\tilde{\Phi}(\eta)$ would require at least three subtractions. It is more convenient to use instead the function

$$\Delta(y) = \Delta_{\log}(y) + \tilde{\Delta}(y), \tag{4.3}$$

where

$$\Delta_{\log}(y) = \tfrac{1}{4}\,y^2. \tag{4.4}$$

The function (4.3) is related to the mismatch between the functions

$$\Phi_{\mathrm{high}}(\eta) = -\frac{\eta^2}{4\pi}\log(-\eta) + \tilde{\Phi}(\eta) \tag{4.5}$$

and

$$\Phi_{\mathrm{low}}(\eta) = -\frac{\eta^2}{4\pi}\log(\eta) + \tilde{\Phi}(\eta) \tag{4.6}$$

at the ray $O-A$. According to the asymptotics (3.35) and (3.36), the function (4.3) exhibits a much slower growth rate, $\Delta(y) \to \Delta_{\mathrm{ass}}(y)$ as $y \to +\infty$, where

$$\Delta_{\mathrm{ass}}(y) = -e^{-i\frac{\pi}{8}}\tilde{G}_1\,y^{\frac{1}{8}}, \tag{4.7}$$

and hence one can write down the dispersion integral with only one subtraction,

$$\tilde{\Phi}(\eta) = \Phi_0 + \tilde{\Phi}_{\log}(\eta) - \frac{\eta}{\pi}\int_{Y_0}^{\infty} \frac{y\, \Re e(e^{\frac{4\pi i}{15}}\varDelta(y)) + \eta\, \Re e(e^{\frac{8\pi i}{15}}\varDelta(y))}{y^2 + 2y\eta\cos(4\pi/15) + \eta^2}\frac{dy}{y}, \tag{4.8}$$

where the term

$$\tilde{\Phi}_{\log}(\eta) = -\frac{Y_0\eta}{4\pi}\cos(4\pi/15) + \frac{\eta^2}{8\pi}\log\left(Y_0^2 + 2\eta Y_0\cos(4\pi/15) + \eta^2\right) \tag{4.9}$$

comes from the domain $0 \leqslant y < Y_0$ in which $\varDelta(y)$ coincides with (4.4).

We will refer to Eq. (4.8) as the "extended dispersion relation." Its validity is equivalent to the validity of the extended analyticity assumption stated above, and under this assumption Eq. (4.8) must hold in the whole complex η-plane, including the shadow domain SHD in Fig. 4.

From (4.8) one readily derives the following expressions for the coefficients of the Taylor expansion (3.29),

$$\Phi_0 = \Re e\left[\frac{e^{\frac{8\pi i}{15}}}{\pi}\int_0^{\infty}\frac{\varDelta(y) - \varDelta_{\text{ass}}(y)}{y}\,dy\right], \tag{4.10a}$$

$$\Phi_1 = -\frac{Y_0}{4\pi}\cos(4\pi/15) - \Re e\left[\frac{e^{\frac{4\pi i}{15}}}{\pi}\int_{Y_0}^{\infty}\frac{\varDelta(y)\,dy}{y^2}\right], \tag{4.10b}$$

$$\Phi_2 = \frac{1}{4\pi}\log Y_0 + \Re e\left[\frac{1}{\pi}\int_{Y_0}^{\infty}\frac{\varDelta(y)\,dy}{y^3}\right], \tag{4.10c}$$

$$\Phi_n = (-)^n\,\Re e\left[\frac{e^{\frac{4\pi i}{15}(2-n)}}{\pi}\int_{Y_0}^{\infty}\frac{(\varDelta(y) - \varDelta_{\log}(y))\,dy}{y^{n+1}}\right] \quad \text{for} \quad n > 2. \tag{4.10d}$$

In Section 8 later we will bring up some numerical evidence to the validity of this extended dispersion relation, thus furnishing a support for the above extended analyticity conjecture.

5. EXCITED STATES. FALSE VACUUM

Although in this work we are mostly interested in the free energy $F(m, h)$, and hence concentrate most of attention on the ground-state energy (2.4) of the finite-size Hamiltonian (2.3), some analysis of excited states will prove to be useful in Section 8, where we study the function $\Phi_{\text{meta}}(y)$. To prepare for this discussion let us briefly remind qualitative properties of the quantum field theory (2.1), in infinite space-time, interpreted as a particle theory.[48]

For $m > 0$ and $h = 0$ (i.e., for $\eta = +\infty$) we have just a free fermion theory (2.2). In this case the vacuum of the bulk theory is two-fold degenerate (the ground states in NS and R sectors degenerate as $R \to \infty$), thus manifesting the spontaneous breakdown of the $\sigma \to -\sigma$ symmetry. The particles (i.e., the free fermions of (2.2)) are identified with the "domain walls." Adding the interaction term in (2.1) creates a confining force between these fermions (which henceforth are refered to as "quarks"), and for nonzero h the particle spectrum contains only their bound states—"mesons." If $m > 0$ and h is small (i.e., η is large positive) the corresponding "string tension" is small ($\sim 2\bar{\sigma}h$, where $\bar{\sigma}$ is the spontaneous magnetization at zero field given by (2.15)), and there is a large number of stable mesons, their masses M_i densely filling the interval between $2m$ and $4m$ (the mesons with $M > 2\,M_1$, M_1 being the lightest meson mass, are generally unstable). In this region of small h the lower part of the meson mass spectrum (with $M_i - 2m \ll m$) can be understood in terms of non-relativistic quarks interacting via a linear confining potential. This interpretation agrees with the result of ref. 48 for the masses of these lightest mesons,

$$M_i - 2m \to \frac{(2\bar{\sigma}h)^{\frac{2}{3}}\, z_i}{m^{\frac{1}{3}}} \qquad \text{as} \quad h \to 0, \tag{5.1}$$

where $-z_i$, $i = 1, 2, 3, \ldots$, are zeroes of the Airy function, $\mathrm{Ai}(-z_i) = 0$. In fact, a few first relativistic corrections to these masses can be computed (see Appendix B),

$$M_i = m\left\{2 + \frac{(2\bar{s})^{\frac{2}{3}}\, z_i}{\eta^{\frac{5}{4}}} - \frac{(2\bar{s})^{\frac{4}{3}}\, z_i^2}{20\eta^{\frac{5}{2}}} + \left(\frac{11 z_i^3}{1400} - \frac{57}{280} + \frac{q_2}{2}\right)\frac{(2\bar{s})^2}{\eta^{\frac{15}{4}}} + O(\eta^{-5})\right\}, \tag{5.2}$$

where the constant q_2 is the same as in Eq. (5.8) later.

As η decreases, the heavier of the mesons gradualy disappear from the spectrum of stable particles; when their masses exceed the stability threshold $2M_1$ they (in general) become resonance states. In particular, when η reaches zero (i.e., $m = 0$), only three stable mesons remain below the threshold; in this case however there are additional five stable particles above the threshold, which owe their stability to the fact that the field theory (1.1) with $\tau = 0$ is integrable.[(9)] This process continues when η

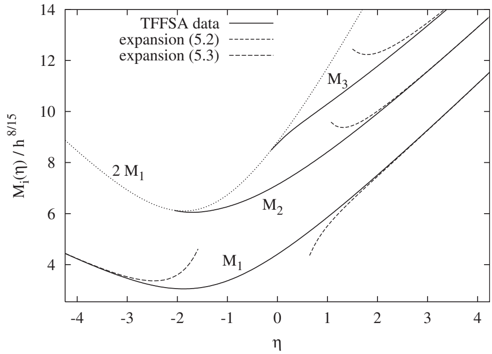

Fig. 5. Masses of the three lighest particles in the Ising field theory (1.1). The solid lines are the plots of the dimensionless ratios $M_i/|h|^{8/15}$ ($i = 1, 2, 3$) versus the parameter (3.19). The dashed lines represent the corresponding large-$|\eta|$ expansions, Eqs. (5.2) and (5.3) (with all terms explicitly written in these Eqs. included).

becomes negative, until finally at $\eta < \eta_2$ ($\eta_2 \approx -2.09$, see Section 6 later) only one particle remains stable. As $\eta \to -\infty$ its mass M_1 approaches $|m|$,[3]

$$M_1 = |m|\,(1 + a/(-\eta)^{\frac{15}{4}} + O((-\eta)^{-\frac{15}{2}})); \qquad a \approx 10.75. \tag{5.3}$$

Although a detailed discussion of the mass spectrum is outside the scope of this paper (we intend to present it separately), we show in Fig. 5 the η dependence of the first few meson masses obtained using the TFFSA.

The mesons described above are excitations over the stable vacuum of the system (which is unique for $h \neq 0$). If $m > 0$ and h is sufficiently small, the system exhibits also an unstable "false vacuum," a global resonance state whose (complex) energy is an intensive quantity, i.e.,

$$E_{\text{meta}} = R\,F_{\text{meta}}(m, h), \tag{5.4}$$

where $R \to \infty$ is the spatial size of the system. The corresponding energy density F_{meta} is a complex-valued quantity, and its imaginary part is interpreted as the decay probability density (the probability per unit volume and unit time) of the false vacuum. According to standard arguments (see refs. 39–41) the resonance energy density $F_{\text{meta}}(m, h)$ coincides with the

[3] The numerical value of the constant a in Eq. (5.3) comes from our estimate

$$a \approx \bar{s}^2 (247/9\,\sqrt{3} - 23/2 + 14/3\pi)$$

of leading ($\sim h^2$) perturbative mass correction. The approximation used in this estimate is similar to that proposed in ref. 37. We will present this calculation elsewhere.

analytic continuation of the vacuum energy density $F(m, h)$ in h, from positive to negative values of h, i.e., it can be written as

$$F_{\mathrm{meta}}(m, h) = \frac{m^2}{8\pi} \log m^2 + |h|^{\frac{16}{15}} \Phi_{\mathrm{meta}}(y), \qquad y = m/|h|^{\frac{8}{15}}, \tag{5.5}$$

where $\Phi_{\mathrm{meta}}(y)$ is the function defined in Section 3. According to (3.18), at small h (i.e., at large y) the imaginary part

$$\Gamma(m, h) = |h|^{\frac{16}{15}} D_{\mathrm{meta}}(y) \tag{5.6}$$

decays exponentially, see Eq. (3.49). In fact, it was argued in ref. 21 that the asymptotic (3.18) itself holds with exponential accuracy provided one replaces $2\bar{\sigma}h \to \Delta F(m, h)$ and $m \to m_q(m, h)$, where

$$\Delta F(m, h) \equiv \Re e\, F_{\mathrm{meta}}(m, h) - F(m, h) \approx 2\bar{\sigma}h + O(h^3), \tag{5.7}$$

is the "string tension," and $m_q(m, h)$ is the "quark mass." Although it is not clear how to give a precise definition to the last quantity, it is natural to assume that at small h it admits an expansion (perhaps, an asymptotic one) in powers of h^2,

$$m_q = m\,(1 + q_2(\bar{\sigma}\, h/m^2)^2 + O(h^4)), \tag{5.8}$$

where q_2 is some constant, whose evaluation constitutes a separate and somewhat involved problem; at the moment we have only a preliminary numerical estimate, $q_2 \approx 0.14(1)$.[4] As the result, the expected asymptotic form of the imaginary part of the function $\Phi_{\mathrm{meta}}(y)$ is

$$D_{\mathrm{meta}}(y) \simeq V(y)(V_0 + V_1 y^{-\frac{15}{8}} + \cdots) \qquad y \to +\infty, \tag{5.9}$$

where $V(y)$ is defined in (3.50), and

$$V_0 = \frac{\bar{s}}{2\pi} = 0.216106\ldots, \qquad V_1 = -\frac{q_2 \bar{s}^2}{2} + \frac{\tilde{G}_3}{4\tilde{G}_1} \approx -0.14. \tag{5.10}$$

In TFFSA we actually study the system in finite-size geometry, with the spatial compactification length R. In this situation the above stable mesons M_i correspond to a series of finite-size energy levels $E_i(R)$ which asymptotically (as $R \to \infty$) behave as

$$E_i(R) = FR + M_i + O(e^{-\frac{\sqrt{3}}{2} M_1 R}), \tag{5.11}$$

---

[4] It results from estimating the three-quark contribution to the quark self-energy; we plan to address this problem separately.

where $F = F(m, h)$ is the vacuum energy density. Of course, there are no resonance states at finite R. If h is sufficiently small, the "false vacuum" resonance of the $R = \infty$ system is very narrow, and at finite R it manifest itself as a peculiar pattern of "near-intersections" of the levels $E_i(R)$, see Fig. 6a in Section 6. The near-intersection of the levels $E_i(R)$ and $E_{i+1}(R)$ occurs approximately at $R_{i,\,i+1} = M_i / \varDelta F$, where $\varDelta F(m, h)$ is the same as in (5.7), and between the two near-intersections the level $E_i(R)$ approximately follows the "resonance" linear law

$$E_i(R) \approx \Re e\, F_{\mathrm{meta}}(m, h)\, R \qquad \text{for} \quad R_{i-1,\,i} < R < R_{i,\,i+1}. \tag{5.12}$$

This pattern (which was previously observed in ref. 49, in the the TCSA study of IFT (1.1)), is clearly visible in Fig. 6a in Section 6. Calculation presented in Appendix B shows that the separation between $E_i(R)$ and $E_{i+1}(R)$ close to their mutual near-intersection follows the square-root law

$$E_{i+1}(R) - E_i(R) \approx mt^2 \sqrt{(mt)^2\,(R - R_{i,\,i+1})^2 + \frac{4\varGamma R}{mt^2 \sigma_i'}}, \tag{5.13}$$

where $\varGamma = \varGamma(m, h)$ is the resonance "specific width," $t = (2\bar{s}\xi)^{1/3}$, and the constants σ_i' are the derivatives of the function $\sigma(\epsilon)$, Eq. (B.16), taken at its zeroes ϵ_i. According to (B.17) and (B.19), these constants have the small-ξ expansions

$$\sigma_i' = \frac{\mathrm{Ai}'(-z_i)}{\mathrm{Bi}(-z_i)} \left\{ 1 + \frac{z_i}{10}\, t^2 - \frac{19 z_i^2}{1400}\, t^4 + O(t^6) \right\}. \tag{5.14}$$

Equation (5.13) will be used in Section 7.3 for the numerical determination of $\varGamma(m, h)$ at small h.

6. NUMERICAL ANALYSIS

In the numerical analysis of the Hamiltonian (2.3) we used the technicaly simplest (albeit may be not optimal) truncation scheme based on the notion of level. We define the level of the state (2.5a) (or (2.5b)) as a half of the sum of absolute values of the half-integers k_i (or the integers n_i). At $m = 0$ this definition coincides with the standard notion of the level in TCSA. The truncation level L is the maximal level of states admitted into the truncated space. For the purposes of this paper we restricted our attention to the zero-momentum sector, i.e., the states with $\sum_i n_i$ or $\sum_i k_i$ equal to zero. For a given truncation level, the Hamiltonian (2.3) was numericaly diagonalized in this sector. We used different truncation levels ranging from 10 to 12; the dimensionality of the truncated spaces then ranges from 487 for $L=10$ to 1186 for $L=12$. This way some number of lowest energy levels $E_i(R)$ was obtained for various real values of h, corresponding to η in the interval $[-5{:}5]$, as well as for pure imaginary h, corresponding to y in (3.37) ranging in the same interval.

6.1. Finite-Size Levels. Qualitative Picture

The qualitative pattern of the resulting finite-size levels $E_i(R)$ is not very sensitive to the truncation level (except for some close proximity of the Yang–Lee point, see below), as long as R is not too large. Of course, higher truncation levels allow for better accuracy in quantitative estimates of its characteristics (energy density and masses). Also, as is usual with truncated Hamiltonians, the truncation effects become more prominent for larger values of R. In quantitative analysis we mostly used the data with $R\,|h|^{\frac{8}{15}}<6$.

6.1.1. Real h

The patterns of the lowest finite-size energy levels $E_i(R)$ for some real η are shown in Figs. 6a–6c. In the range of R shown in these figures the difference between the plots for $L=10$ and $L=12$ would not be visible. Qualitatively, the patterns in Figs. 6a–6c are the same as were observed in ref. 49 in the TCSA study of (1.1), where their interpretations in terms of the particle spectra are discussed. In this case, we have just a few words to add.

In full accordance with the McCoy and Wu scenario,(48) for sufficiently large positive η (i.e., for $T<T_c$ and small h) the field theory (1.1) contains a large number of stable particles ("mesons"). At finite R, these particles correspond to the energy levels $E_i(R)$ which approach, at sufficiently large R, the straight lines $F(m,h)\,R+M_i$, where M_i are the masses of the mesons. This pattern of levels is clearly visible in the plot of Fig. 6a representing the case of $\eta=2.2$. For sufficiently large η the meson masses M_i are in good agreement with (5.2) (see Fig. 5). The plot in Fig. 6a also shows a characteristic pattern of "near intersections" of the meson levels with the straight line $\Re e\, F_{\text{meta}} R$, which is the finite-size manifestation of the "false vacuum" already mentioned in Section 5. As is discussed there and in Appendix B, the openings at these near-intersections are related to the imaginary part (5.6) of the "false vacuum" specific energy, see Eq. (5.13). We will use this relation in Section 8 as a way to estimate the resonance width at sufficiently large positive η.

As η decreases, the mesons with higher masses gradually disappear into the "continuum" above the the stability threshold $2M_1$, where M_1 is

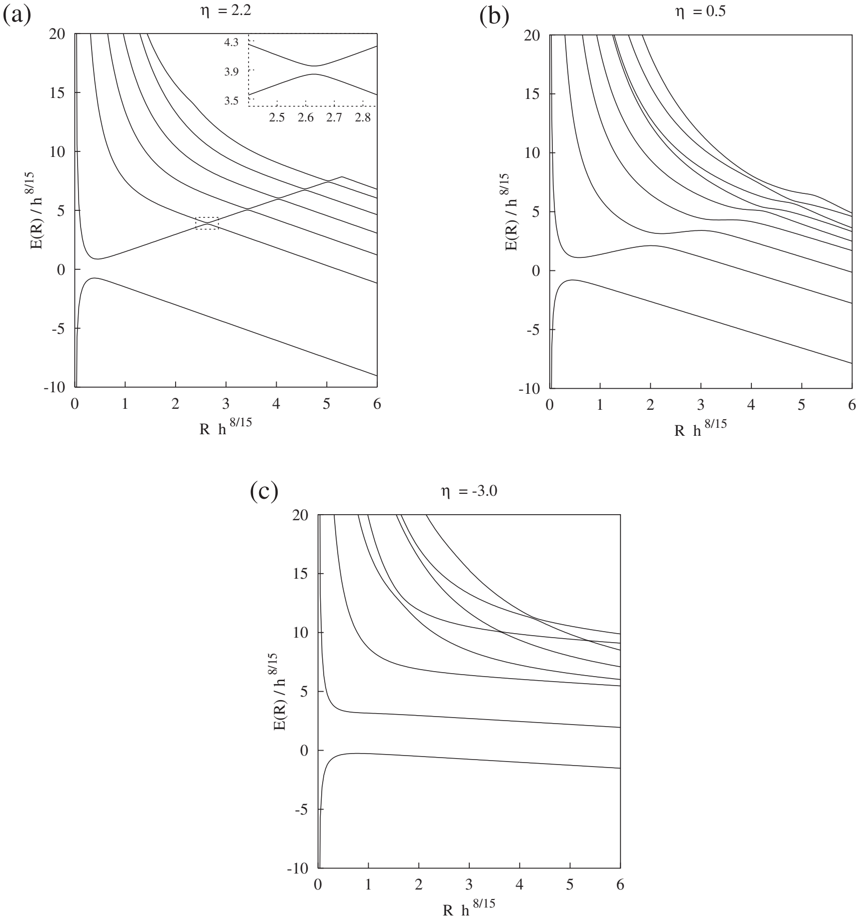

Fig. 6. Plots of several lowest energy levels $E_i(R)$, $i = 0, 1, 2, \ldots$, at different η. (a) $\eta = 2.2$. Magnification in the corner shows the "near-intersection" of the levels $E_1(R)$ and $E_2(R)$. (b) $\eta = 0.5$. Three lowest excited levels $E_1(R)$, $E_2(R)$, $E_3(R)$ are seen to approach straight lines (5.11) exponentially; these levels correspond to three stable mesons M_1, M_2, M_3. The rest of the levels correspond to scattering states. (c) $\eta = -3.0$. Only one stable particle remains.

the mass of the lightest particle (see Fig. 6b, where only three stable particle levels are apparent). At the same time the resonance "level" becomes fussy, in agreement with the expectation that its width parameter Γ grows. The process of depletion of the "meson" spectrum continues as η decreases to negative values. The third lightest particle disapears at $\eta \approx -0.14$, and the second one leaves the spectrum of stable particles at $\eta = \eta_2$,

$$\eta_2 = -2.09(4). \tag{6.1}$$

The way these particles disapear is an interesting question which we hope to address elsewhere. For η below η_2 only one particle with mass M_1 is left, as is manifest in Fig. 6c. The η-dependence of the first three masses was shown in Fig. 5. We postpone a detailed quantitative discussion of the particle spectrum to future publication.

6.1.2. Pure Imaginary h

Much different patterns of the finite-size energy levels appear if one takes h pure imaginary, which corresponds to $\eta = y e^{\frac{4\pi i}{15}}$ with real y. Although in this case the Hamiltonian (2.3) is not an Hermitian operator, it has an explicit symmetry

$$SHS = H^{\dagger}, \tag{6.2}$$

where the operator S just flips the signs of all states in the R sector in (2.5b). As the result, the eigenvalues of this Hamiltonian are either real or come in complex conjugated pairs.

For sufficiently large negative y the ground state energy $E_0(R)$ of the truncated Hamiltonian remains real in a wide range of R, including the region where the linear behaviour (2.4) is already clearly visible. This is also true for the first excited level $E_1(R)$, which quickly (i.e., exponentialy) approaches the straight line $FR + M_1$, i.e., it behaves as a one-particle state with a real mass M_1. The situation is exemplified in Fig. 7a, where the real parts of the first few energy levels are plotted.

As y increases, the gap M_1 becomes smaller (see Fig. 7b), and for y above -2.43 a collision of the first two levels at some finite $R = R_{\text{nose}}(y)$ (the "nose") is clearly visible; at $R > R_{\text{nose}}(y)$ the levels $E_0(R)$ and $E_1(R)$ form a complex-conjugated pair, as is seen in Fig. 7c. When y furher increases, the "nose" quickly gets shorter, and when it is short enough (as in Figs. 8a–8b) it becomes evident that for large $R \gg R_{\text{nose}}$ the complex conjugate levels $E_0(R)$ and $E_1(R)$ develop into the "straight lines" with complex slopes, $E_0 \to FR$, $E_1(R) \to F^*R$. We interpret this as the vacuum state acquiring a complex energy density F (obviously, in this case there are two "complex conjugate" vacua). Moreover, the next lowest levels $E_2(R)$ and $E_3(R)$ eventualy collide and they too become a complex conjugate pair, both then approaching similar straight lines, shifted by some complex "mass" M_1, i.e., $E_2(R) \to FR + M_1$, $E_3(R) \to F^*R + M_1^*$; these levels are naturaly interpreted in terms of the complex-mass particle-like excitations over the corresponding vacua.

As y becomes larger the number of such complex-mass particles increases. Higher energy levels form a rather complicated pattern. Their interpretation in terms of particle scattering states (and even legitimacy of

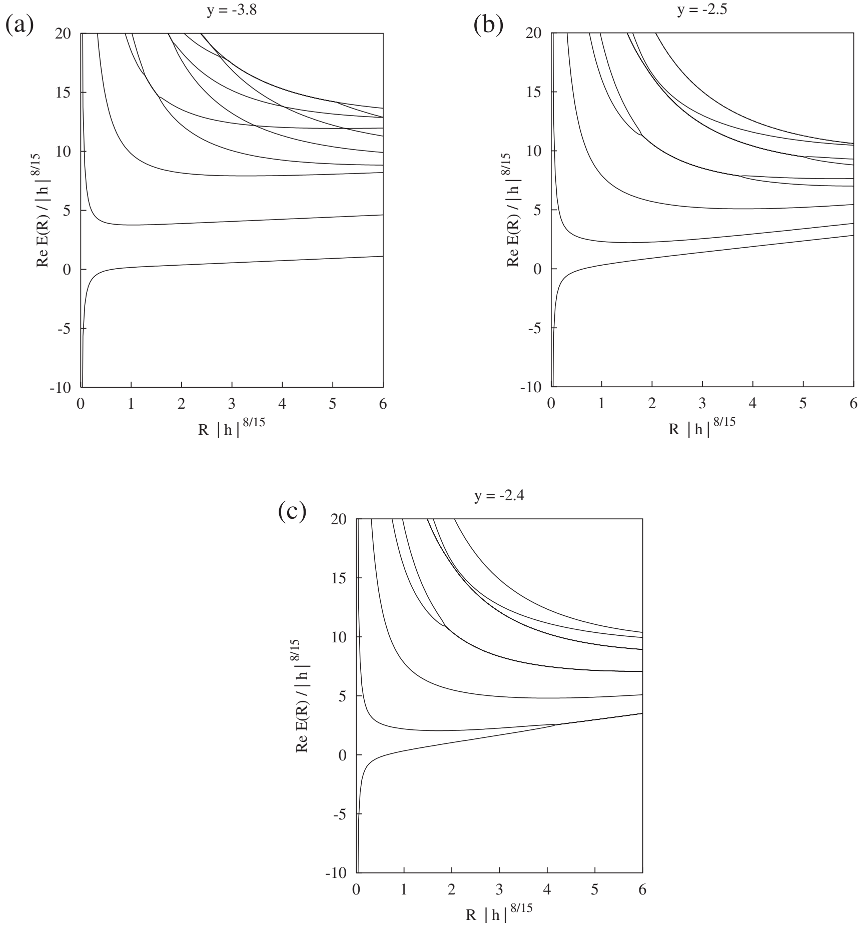

Fig. 7. Plots of several lowest energy levels $E_i(R)$, $i = 0, 1, 2, \ldots$, at pure imaginary h, i.e., at $\eta = y \exp(4\pi i/15)$ with real y. When a level becomes complex, only its real part is shown. (a) $y = -3.8$. The three lowest levels $E_0(R)$, $E_1(R)$, $E_2(R)$ are real for all $R\,|h|^{\frac{8}{15}} \in [0;6]$. The level $E_1(R)$ approaches the straight line $FR + M_1$ exponentially; it corresponds to one-particle state. (b) $y = -2.5$ (close to the Yang–Lee point $Y_0 \approx -2.43$). The three lowest levels remain real for all $R\,|h|^{\frac{8}{15}} \in [0{:}6]$, but the gap between $E_0(R)$ and $E_1(R)$ narrows. (c) $y = -2.4$ (on the other side of the YL point). The "nose" appears: $E_0(R)$ and $E_1(R)$ collide at $R = R_{\text{nose}} \approx 4.3\,|h|^{-8/15}$ and become a pair of complex-conjugated levels at $R > R_{\text{nose}}$.

such interpretation) in general remains an open problem which we hope to address in the future.

Appearence of complex F for y above the Yang–Lee point $-Y_0$ is well expected in view of the discussion in Section 3; F and F^* are just the values of $F(m, h)$ on two edges of the branch cuts in Fig. 1. We can say that the

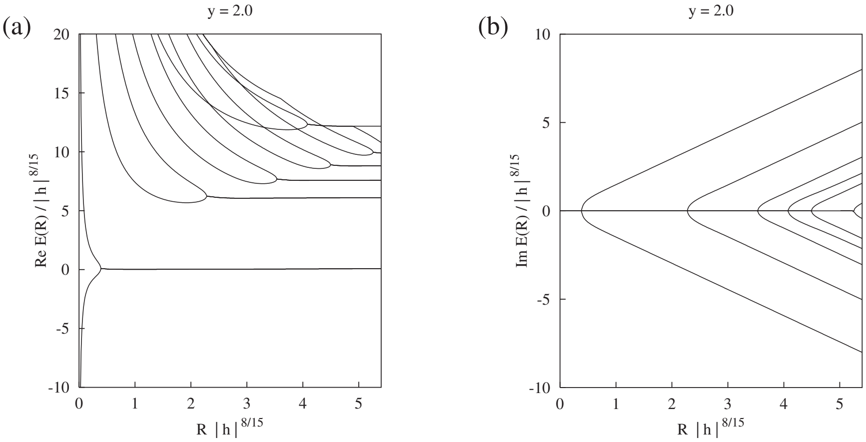

Fig. 8. The lowest energy levels $E_i(R)$, $i = 0, 1, 2, \ldots$, at $\eta = 2.0 \times e^{4\pi i/15}$. (a) Real parts of $E_i(R)$. (b) Imaginary parts of $E_i(R)$. Two lower levels, E_0, E_1, collide at $R = R_{\mathrm{nose}} \approx 0.389\, |h|^{-\frac{8}{15}}$ becoming at larger R a complex-conjugated pair. They quickly approach straight lines, whose slopes are interpreted as F and F^*. Similar collision of the next two levels, E_2, E_3, occurs at $R \approx 2.28\, |h|^{-\frac{8}{15}}$; they also develop into two complex-conjugated straight lines, with the same slopes as F and F^*. The gap $E_2(R) - E_0(R)$ approaches a complex constant M_1, interpreted as a complex mass (correspondingly, the gap $E_3(R) - E_0(R)$ approaches M_1^*).

patterns in Fig. 7b and in Fig. 7c represent the situations at the opposite sides of the Yang–Lee edge singularity, which is located some place in between. Unfortunately (but not surprisingly), in the close proximity of this critical point the results from the truncated Hamiltonians appear to be more sensitive to the truncation level then elsewhere, especialy for larger

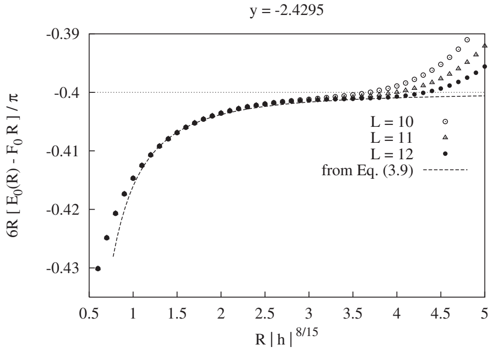

Fig. 9. The function $C_0(R) = 6R[E_0(R) - 0.54743\, |h|^{\frac{16}{15}} R]/\pi$ computed through the TFFSA using different truncation levels $L = 10$, 11, 12, at $\eta = -2.4295 \times e^{4\pi i/15}$. The dotted line is the expected asymptotic value $-c_{\mathrm{eff}} = -0.4$. The dashed line represents the two leading corrections written in Eq. (3.9) with $\alpha_0 = -4.2$.

values of R. In Fig. 9 we show the plots of the function $C_0(R) \equiv \frac{6R}{\pi}(E_0(R) - F_0 R)$, with

$$F_0 \approx 0.54743\,|h|^{16/15}, \tag{6.3}$$

computed for different truncation levels, at $y = -2.4295$ (which we believe to be very close to the Yang–Lee point $-Y_0$). As the truncation level increases it seems to develop the expected large-R behaviour (3.9).

6.2. Quantitative Analysis

The free energy $F(m, h)$ was determined by measuring the slope of the R dependence of the ground sate level $E_0(R)$ at sufficiently large R. There are two obstacles (well known in TCSA) to a precise determination of this slope. Theoretically, the linear behaviour (2.4) becomes exact for large $R \gg M_1^{-1}$, while at finite values of R finite-size corrections may be important. Although the leading finite-size corrections are related to the masses M_i of the stable particles by well-known formula (see, e.g., ref. 17)

$$E_0(R) = RF(m, h) - \sum_i \frac{M_i}{\pi} K_1(M_i R) + O(e^{-2M_1 R}), \tag{6.4}$$

where $K_1(x)$ is modified Bessel function, the subleading corrections depend on the (generally unknown) scattering amplitudes, and in most cases it is not clear how to take them into account. This makes it favorable to use larger values of R, where these subleading finite-size corrections are less significant. However, in practical calculations the ground-state energy deviates from the linear behaviour (2.4) at large R as the result of the state space truncation (the "truncation effects"). Although this deviations are too small to be visible in Figs. 6–8, they substantially reduce the precision of quantitative analysis. The truncation effects bring an upper limit to the values of R at which precise quantitative analysis can be made.

To reduce the truncation effects, the ground-state energy functions $E_0^{(L)}(R)$ computed with the truncation levels $L = 10, 11, 12$ was extrapolated to $L \to \infty$. The extrapolation was made by fitting the formula

$$E_0^{(L)}(R) = s_0(R) + s_1(R)\, L^{-s_2(R)} \tag{6.5}$$

to the computed L dependence (at fixed R), via s_0, s_1, s_2, and accepting $s_0(R)$ as the extrapolated $E_0(R)$. Although this formula does not have theoretical justification, the extrapolation procedure appears to work well for all real as well as imaginary h, corresponding to $|\eta| < 5$, substancially improving the linear shape of $E_0(R)$ (e.g., for $R \sim 20M_1^{-1}$ the deviation from the linear behaviour is reduced by at least one order of magnitude).

The extrapolated function $E_0(R)$ was then subjected to a finite-size analysis. The masses M_i of the stable particles were estimated from the higher levels $E_i(R)$, and the expected leading finite-size corrections (the sum in (6.4)) were subtracted from $E_0(R)$.

For negative η in Table IV we subtracted all one-particle corrections and then used the function $f_0 R + f_1 \exp(-2 f_2 R)$ to fit (around $R \approx 4M_1^{-1}$) the remaining part via f_0, f_1, f_2, with the best-fit value of f_0 accepted as $F(m, h)$. For positive η we subtracted instead the corrections from the two lightest particles and then used $g_0 R + g_1 K_1(g_2 R)$ to fit the resulting curve (around $R \approx 7M_1^{-1}$). The overall quality of this analysis was controlled by observing the proximity of the best-fit value of f_2 and g_2 to the expected values $2M_1$ and M_3, respectively (the deviation varied with η, but never exceeded 20%).

The above procedure of the finite-size analysis is rather labor consuming. In order to obtain estimates of the coefficients Φ_n we used similar procedure in the small interval $[-0.64 : 0.64]$ around zero but we only subtracted the lighest particle correction before fitting to $g_0 R + g_1 K_1(g_2 R)$ around $R \approx 8M_1^{-1}$.

Table IV. Numerical Values of $\Phi(\eta)$ at Selected Real Points. The First Column Shows Direct Data Obtained Through TFFSA, as Explained in Section 6.2; We Believe These Numbers Are Exact to Six Significant Digits or Better. The Results from High-T and Low-T Dispersion Relations, Eqs. (8.1) and (8.9), with the Use of Approximations (8.2) and (8.14), Are Presented in the Second and the Third Columns, Respectively. The Last Column Contains Results from Extended Dispersion Relation, Eq. (4.8), with Approximation (8.21) Used

$\Phi(\eta)$	From TFFSA data	From high-T disp. relation	From low-T disp. relation	From extended disp. relation
$\Phi(-5)$	−0.1092101	−0.1092092	—	−0.1088626
$\Phi(-4)$	−0.1592682	−0.1592643	—	−0.1589421
$\Phi(-3)$	−0.2529928	−0.2529887	—	−0.2527417
$\Phi(-2)$	−0.4413450	−0.4413249	—	−0.4412136
$\Phi(-1)$	−0.7839665	−0.7839668	—	−0.7839576
$\Phi(0)$	−1.1977330	—	—	−1.1977320
$\Phi(1)$	−1.3898410	—	−1.3898417	−1.3898063
$\Phi(2)$	−1.4930558	—	−1.4930566	−1.4929849
$\Phi(3)$	−1.5642732	—	−1.5642736	−1.5641727
$\Phi(4)$	−1.6188506	—	−1.6188510	−1.6187275
$\Phi(5)$	−1.6632483	—	−1.6632485	−1.6631076

We believe that the data for $F(m, h)$ obtained through this procedure are exact to six significant digits.

Finally, massive data used in Fourier analysis in Section 8.2.1 was obtained using somewhat simplified procedure, in which only the first term in the sum (6.4) was taken into account, i.e., no subtraction was performed. Specifically, the function $g_0 R + g_1 K_1(g_2 R)$ was fitted to the extrapolated data $E_0(R)$. This procedure produces the estimates which agree with the above more elaborate analysis to five significant digits.

Similar simplified analysis was used in the case of pure imaginary h. In this case, for $y > -Y_0$, complex values of the fitting parameters g_0, g_1, g_2 were admitted. Exceptionally, for the values on the side $y < -Y_0$ presented in Table V, we subtracted the leading finite size correction and then fitted to $g_0 R + g_1 \exp(-g_2 R)$. Special was the vicinity of the critical point $-Y_0$. With y approaching this point the values of g_2 decreased and overall quality of the fit deteriorated. Of course this is not surprising since near the critical point the correlation length M_1^{-1} is diverging, pushing the domain of validity of the expansion (6.4) to $R \to \infty$, where our analysis would be severely spoiled by truncation effects. Nonetheless, it was possible to obtain reasonably accurate data (at least four digits) for $\Phi_{\text{imh}}(y)$ with $y < -2.43$. On the other side of the critical point, for $y > -Y_0$, the situation is complicated by the rapid growth of the "nose." In this region we could obtain similar accuracy only for $-2.1 < y$, and our data for $-2.3 < y < -2.1$ may be less accurate. In close vicinity of the critical point a finite-size analysis based on the effective action (3.7) would be more appropriate, and we are planning to apply it in the future.

Table V. Numerical Values of $\Phi_{imh}(y)$, Eq. (3.37), at some Real $y < -Y_0$. Direct Data from TFFSA (Good to Four Digits or Better, See Section 6.2) Are in First Column, and Results from High-T Dispersion Relation with (8.2) in Second Column

$\Phi_{\text{imh}}(y)$	From TFFSA data	From high-T disp. relation
$\Phi_{\text{imh}}(-5.0)$	0.1116003	0.1115969
$\Phi_{\text{imh}}(-4.5)$	0.1349420	0.1349380
$\Phi_{\text{imh}}(-4.0)$	0.1674520	0.1674469
$\Phi_{\text{imh}}(-3.5)$	0.2155503	0.2155426
$\Phi_{\text{imh}}(-3.0)$	0.2946233	0.2946092
$\Phi_{\text{imh}}(-2.5)$	0.4729294	0.4728305
$\Phi_{\text{imh}}(-2.4295)$	—	0.5475373

7. NUMERICAL RESULTS

7.1. Scaling Function. Real h

Our results for $\Phi(\eta)$ at real values of η are shown in Fig. 10 (see also Table IV for some numerical values). As expected (see Section 3), the function appears to be perfectly smooth everywhere exept for the point $\eta = 0$, where the singularity of the form $-\eta^2 \log \eta^2/8\pi$ can be observed. The first few coefficients of the η-expansion (3.29) can be readily extracted from this data. After subtracting the above singular term, we have fitted polynomials of various degree to the data in the interval $[-0.64 : 0.64]$. The fit appears stable for the first eight coefficients, Φ_0 to Φ_7. The resulting estimates of these coefficients are displayed in Table III. The estimates for the coefficients Φ_0 and Φ_1 are very close to the predictions (3.31) and (3.33); this result for Φ_1 can be viewed as numerical verification of the exact expectation value $\langle \epsilon \rangle |_{\tau=0}$ obtained in ref. 43. It turns out that the first few terms of the series (3.29) provide rather good approximation for $\Phi(\eta)$ with $|\eta| \lesssim 2$, as shown in Fig. 10. Comparison with the known terms of the expansions (3.35) and (3.36) is also presented in that figure.

7.2. Scaling Function. Imaginary h

Our results for $\Phi_{\text{imh}}(y)$ are shown in Fig. 11, where a singularity at $y = -Y_0$,

$$Y_0 \approx 2.4295, \tag{7.1}$$

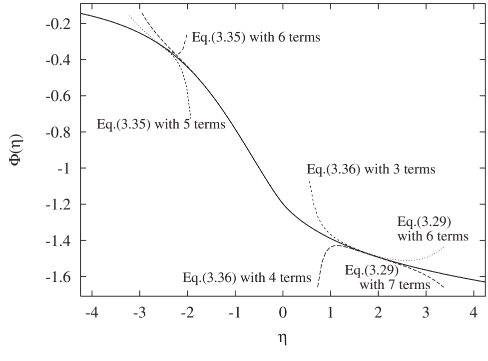

Fig. 10. The scaling function $\Phi(\eta)$ for real η (solid line). Dashed lines show how this function is approximated by few leading terms of the expansions (3.29), (3.35), and (3.36).

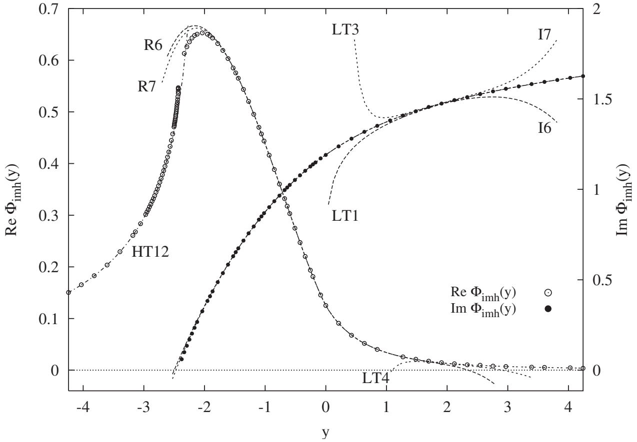

Fig. 11. The TFFSA data for the function $\Phi_{\mathrm{imh}}(y)$, Eq. (3.37) (empty and full bullets). The imaginary part $\Im m\, \Phi_{\mathrm{imh}}(y)$ vanishes for $y < -Y_0$. Various dashed lines show how this function is approximated by its expansions (3.29), (3.35), and (3.36). I6 and I7 are the first seven (including $\bar{\Phi}_6\, y^6$) and eight (including $\bar{\Phi}_7\, y^7$) terms of (3.43). Corresponding expansions of the real part are the lines R6 and R7. One, three, and four terms of the asymptotic expansion (3.36) are shown as LT1, LT3, and LT4, respectively (obviously, only even (odd) terms contribute to the real (imaginary) part). Finally, HT12 is the plot of six leading terms (including G_{12} term) of the low-T expansion (3.35). In all cases the coefficients are taken (or computed) from Tables I, II, and III.

is clearly visible. The function $\Phi_{\mathrm{imh}}(y)$ is real for $y < Y_0$, and it develops an imaginary part for $y > Y_0$. A comparison with the first few terms of the expansions (3.35) and (3.36) is also made in the Fig. 11. We observe that the first six terms of (3.35) approximate $\Phi_{\mathrm{imh}}(y)$ very well for $y < -2.7$. This is not surprising since, according to our discussion in Section 3, the expansion (3.35) is expected to converge for all $y < Y_0$. In this figure we also compare the data with the first eight terms of the expansion (3.43) (and similar expansion for the real part of $\Phi_{\mathrm{imh}}(y)$). One can notice that these expansions provide a remarkably good approximation of $\Phi_{\mathrm{imh}}(y)$ for $|y| < 2$. We take this as an indication that it is the Yang–Lee singularity at $\eta = -Y_0 e^{\pm\frac{4\pi i}{15}}$ which determines the domains of convergence of the small η expansion (3.29); in other words, it supports our expectation that the function $\tilde{\Phi}(\eta)$ is analytic in the whole disk $|\eta| < Y_0$.

Our data agree with the expected form (3.40) of the singularity at $y = -Y_0$. The imaginary part of $\Phi_{\mathrm{imh}}(y)$, Eq. (3.39), receives no contribution from the regular part $A(y)$ in (3.40), and therefore it should exhibit the singular behaviour (3.40) most prominently. The log-log plot of this function in Fig. 12a clearly confirms the value $5/6$ of the exponent in (3.40) predicted in ref. 30. The ratio $\Im m\, \Phi_{\mathrm{imh}}(y)/(y + Y_0)^{\frac{5}{6}}$ is shown in Fig. 12b.

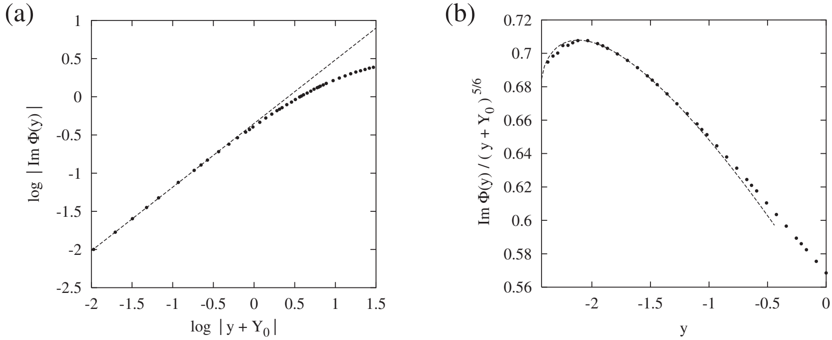

Fig. 12. TFFSA data for $D_{\mathrm{imh}}(y)$, Eq. (3.39). (a) Log-log plot of $D_{\mathrm{imh}}(y)$ (bullets). The dashed line has slope 5/6. (b) Ratio $D_{\mathrm{imh}}(y)/(y+Y_0)^{5/6}$ (bullets), and the graph of $D^{<}_{\mathrm{imh}}(y)/(y+Y_0)^{5/6}$, with $D^{<}_{\mathrm{imh}}(y)$ from Eq. (8.3) (dashed curve).

This plot reveals the "fine structure" of this function near the Yang–Lee branching point, which should be attributed to the subleading singular terms in (3.40). Our data is not very precise when taken close to the critical point $-Y_0$ (see Section 6), and allow for only rather rough estimate of the leading coefficients in the expansion (3.40), (3.41),

$$B_0 = -1.37(2), \qquad B_1 = -0.75(5), \qquad C_0 = 0.38(7), \tag{7.2a}$$

$$A_0 = 0.5474(3), \qquad A_1 = 1.06(4), \qquad A_2 = 0.3(1). \tag{7.2b}$$

These estimates are obtained by fitting a few leading terms of (3.41) to the data in various intervals of y between -2.2 and -1.5; the error reflects the dependence on the fitting interval as well as on the number of the terms used. From (7.2a) we can obtain an estimate of the most important parameters in (3.8a), (3.8b),

$$\lambda_1 = 3.10(6), \qquad \alpha_0 = -4.9(9). \tag{7.3}$$

Independent (and somewhat better) estimate of the parameter α_0 can be obtained directly from the finite-size ground-state energy $E_0(R)$ at the Yang–Lee point $y = -Y_0$. By fitting the expected form (3.9) to the data in Fig. 9 in various regions between $R = 1.7\,|h|^{-\frac{8}{15}}$ and $R = 2.8\,|h|^{-\frac{8}{15}}$ we found

$$\alpha_0 = -4.4(4), \tag{7.4}$$

(where again the error estimate is from the dependence on the fitting region). The quality of the fit is also shown in Fig. 9.

7.3. False Vacuum Resonance Width

As was discussed in Section 5, the finite-size behaviour of the meson levels close to their "near-intersection" points is related through (5.13) to the width Γ of the false vacuum resonance, and can be used for numerical determination of $D_{\text{meta}}(y)$. Presently, there are two limitations to this approach. First, at small h the "near- intersections" occur at large R, where truncation effects are more significant. In our calculations, a satisfactory stabilization of the difference $E_2(R)-E_1(R)$ at $L=12$ was achieved only for $\eta<3.5$. For larger η the situation can be somewhat improved by adding a number of two-quark states of higher levels (see below). On the other side of large h, a limitation comes from our unsufficient knowledge about the coefficients σ_i' in (5.13); the best we have at the moment is the first three terms (5.14) of their small-h expansions. Nevertheless, one can note that these three terms were obtained in Appendix B within the same approximation as the three correction terms in the large-η expansion of the meson masses, Eq. (5.2). Good agreement of the last expansion with the data at $\eta>1.7$ makes us believe that reasonably accurate estimate of the function $D_{\text{meta}}(\eta)$ can be obtained within this expansion in the same region.

We have performed this analysis in the range $1<\eta<4.5$ using the separation $E_2(R)-E_1(R)$. The eigenvalues $E_1(R)$, $E_2(R)$ were computed in "two-quark extended" truncated space (2.5) with $L=12$. Namely, besides all states in (2.5) with $L\leqslant 12$, the two-quark states $a_k^\dagger a_{-k}^\dagger\,|\,0\rangle_{\text{NS}}$ and $a_n^\dagger a_{-n}^\dagger\,|\,0\rangle_{\text{R}}$ with the levels $12<L\leqslant 100$ were also admitted. While such extention does not bring any appreciable difference for $\eta\leqslant 3.5$, it does substantially improve the results for $3.5<\eta<4.5$. For all values of η in the range $1<\eta<4.5$ the separation $E_2(R)-E_1(R)$ was in excellent agreement with the expected square-root behaviour (5.13), and it allowed us to estimate the values of the width parameter Γ. The results for the ratio $D_{\text{meta}}(y)/V(y)$ (where $D_{\text{meta}}(y)$ is related to Γ through (5.6), and $V(y)$ is the function (3.50)) are shown in Fig. 13. The ratio shows a clear tendency to approach at large y the expected value $V_0=0.2161\ldots$. Moreover, when all three terms in (5.14) are taken into account, for $y>2.3$ it agrees well with the first correction term in (5.9). By direct fitting the expansion (5.9) to this data we have obtained the following estimates of the coefficients there,

$$V_0=0.2161(4),\qquad V_1=-0.136(4). \tag{7.5}$$

In ref. 42 an attempt was made to determine the $h\to 0$ behaviour of Γ using two-quark approximation for the resonance wave function. While correctly reproducing the exponent in (3.18), this calculation yields somewhat greater pre-exponential factor $\pi\bar{\sigma}h/18$ (which would lead to

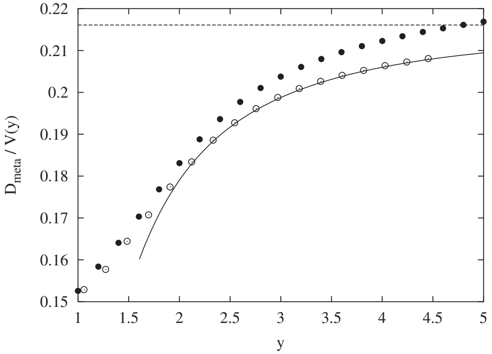

Fig. 13. Data for the ratio $D_{\mathrm{meta}}(y)/V(y)$ obtained through the false vacuum resonance width analysis (Section 7.3), using Eq. (5.13) with three leading terms in Eq. (5.14). The data obtained using "two-quark extended" truncation space with the truncation level $L=12$ is shown as empty bullets (⊙). The data obtained using two-quark states *only* is shown as full bullets (●). The solid line is the plot of Eq. (8.11) and the dotted line is the value $V_0 = 0.2161$.

$V_0 = \pi\bar{s}/18 \approx 0.237$ in our notations). As we explain in Appendix B, the two-quark approximation breaks down when the quarks are deep inside the classically unaccessible region, and therefore it is not justified in the resonance wave function calculation even at $h \to 0$, even though in this limit the resonance decay goes predominantly through the two-quark channel.[5] To verify this being the reason for the above discrepancy, we have repeated the calculation described in this section, this time with the eigenvalues $E_1(R), E_2(R)$ computed purely within the two-quark approximation. Specifically, in computing these eigenvalues, *only* two-quark states with the levels $\leqslant 100$ were admitted. As is seen in Fig. 13, the ratio $D_{\mathrm{meta}}(y)/V(y)$ obtained this way is hardly consistent with the correct $y \to \infty$ asymptotic value 0.2161....

8. ANALYTICITY

8.1. High-T Domain (HTW in Fig. 4)

In principle, our approach allows for direct computation of the function $\Phi(\eta)$ at complex values of η in the wedge HTW in Fig. 4. However, this data would be redundant because in view of the analytic properties of

---

[5] To avoid misunderstanding let us stress here that in Appendix B we apply the two-quark approximation to the wave function in the "meson domain," not deep under the barrier. Instead of solving the problem in the last region, we take a phenomenological approach based on the Breit–Wigner formula (B.23).

the scaling function discussed in Section 3, the values of $\Phi(\eta)$ can be computed through the dispersion relation (3.3) once the function $D_{\rm imh}(y) \equiv \Im m\,\Phi_{\rm imh}(y)$ is known. This dispersion relation applies to the function $\Phi(\eta)$ with η in the wedge HTW in Fig. 4, where it can be rewritten as

$$\Phi(\eta) = -\frac{15\eta^2}{4\pi}\int_0^{Y_0} \frac{D_{\rm imh}(-y)\, y^{\frac{3}{4}}\, dy}{y^{\frac{15}{4}} + (-\eta)^{\frac{15}{4}}}. \tag{8.1}$$

Since accurate direct data on $D_{\rm imh}(y)$ in the vicinity of the Yang–Lee point $(-Y_0 < y < 2.1)$ is not available at this moment, some extrapolation is needed in order to perform the (numerical) integration in (8.1). We have tried various extrapolations, and the results of integration in (8.1) usualy agree with the our direct data on $\Phi(\eta)$ to at least three significant digits. The best results were obtained with the following approximation

$$D_{\rm imh}(y) = \begin{cases} D^{<}_{\rm imh}(y) & \text{for} \quad -Y_0 < y < -1.57; \\ D^{>}_{\rm imh}(y) & \text{for} \quad -1.57 < y < 0, \end{cases} \tag{8.2}$$

where

$$D^{<}_{\rm imh}(y) = -\frac{1}{2}\,\bar{B}_0(y+Y_0)^{\frac{5}{6}} + \frac{1}{2}\,\bar{B}_1(y+Y_0)^{\frac{11}{6}} + \frac{\sqrt{3}}{2}\,\bar{C}_0(y+Y_0)^{\frac{5}{3}}, \tag{8.3}$$

with

$$\bar{B}_0 = -1.3693, \qquad \bar{B}_1 = -0.74378, \qquad \bar{C}_0 = 0.42446, \tag{8.4}$$

and $D^{>}_{\rm imh}(y)$ is just the first eight terms of the y-expansion,

$$D^{>}_{\rm imh}(y) = \bar{\Phi}_0 + \bar{\Phi}_1\, y + \cdots + \bar{\Phi}_7 y^7. \tag{8.5}$$

with $\bar{\Phi}_n$ related to Φ_n from the Table III as in (3.44). Here we accept (7.1) as the value of Y_0, while the coefficients $\bar{B}_0$, $\bar{B}_1$, $\bar{C}_0$ in (8.4) are obtained by exact matching (8.3) with (8.5) at $y = -1.57$ (up to the first derivative), and fine-tuning the remaining one parameter to achieve better agreement with the data. Note that these coefficients agree with the estimate (7.2a) within the stated accuracy. However, (8.4) should not be considered as better estimates of the coefficients of the expansions (3.41b)–(3.41c), since (8.3) ignores higher subleading terms in (3.40). The quality of the approximation (8.2) is demonstrated in the Tables IV and V, where the results from (8.1) are compared to our data, both for real $\eta < 0$ and $\eta = y\, e^{\frac{4\pi i}{15}}$, $y < -Y_0$. We also presented in Table I the results for the first few coefficients G_{2n} in (3.1) obtained through the dispersion relation (3.5) with the use of (8.2). The agreement with the previously known estimates is reasonable, baring in mind relatively low quality of the approximation (8.3); we believe it will improve once the structure of singular expansion (3.40) is understood in greater quantitative details.

8.2. Low-T Domain (LTW in Fig. 4)

8.2.1. Fourier Analysis

Numerical analytic continuation into this domain was performed using Fourier analysis in the logarithmic variable $\log\eta$. According to (3.29) and (3.36) the function $\eta^{\frac{13}{16}}(\Phi(\eta)-\tilde{G}_1\,\eta^{\frac{1}{8}})$ decays sufficiently fast (exponentially in the above logarithmic variable) both at $\eta\to 0$ and at $\eta\to\infty$. Its logarithmic Fourier transform

$$\Psi(\omega)=\int_0^{\infty}\eta^{\frac{13}{16}-i\omega}\,(\Phi(\eta)-\tilde{G}_1\eta^{\frac{1}{8}})\,\frac{d\eta}{\eta} \tag{8.6}$$

was evaluated numerically from our data for $\Phi(\eta)$. In principle, using this function the values of $\Phi_{\text{low}}(\eta)$, Eq. (4.6), along the rays $\eta=ye^{i\alpha}$, with real $y\in(0,+\infty)$, can be computed as the inverse Fourier transforms

$$\Phi_{\text{low}}(ye^{i\alpha})=\tilde{G}_1\,e^{i\frac{\alpha}{8}}y^{\frac{1}{8}}+e^{-i\frac{13}{16}\alpha}y^{-\frac{13}{16}}\int_{-\infty}^{\infty}e^{-\alpha\omega}\Psi(\omega)\,y^{i\omega}\,\frac{d\omega}{2\pi}. \tag{8.7}$$

The function $\Phi_{\text{low}}(\eta)$ is analytic along the ray provided the integrand in (8.7) decays faster then any power of ω. The standard analyticity assumption for the wedge LTW in Fig. 4 is equivalent to the statement that $|\Psi(\omega)|<\exp(-\frac{8}{15}\pi\,|\omega|)$ for $|\omega|\to\infty$. Of course it is not possible to achieve a rigorous conclusion about true large ω asymptotic of this function using our limited-precision data. For $\omega>\omega_{\max}\sim 5.5$ the numerical Fourier transform $\Psi(\omega)$ is dominated by a small ($\sim 10^{-6}$) random-looking function which should be interpreted as the Fourier transform of the errors associated with our numerical data for Φ. For this reason the numerical Fourier transform $\Psi(\omega)$ hardly carries any usefull information beyond the window $|\omega|<\omega_{\max}$. At the same time the function $\Psi(\omega)$ inside this window appears to be decaying significantly faster then the above exponential, which is consistent with the standard analyticity assumption. One can actually use (8.7) to compute this function in LTW with reasonable accuracy. Obviously, in order to do that one has to introduce some cut-off to eliminate the high frequency part $|\omega|>\omega_{\max}$ of the integral (8.8) dominated by the noise; it is expected that only fine details of the resulting function would depend on the specifics of the cutoff procedure. As an

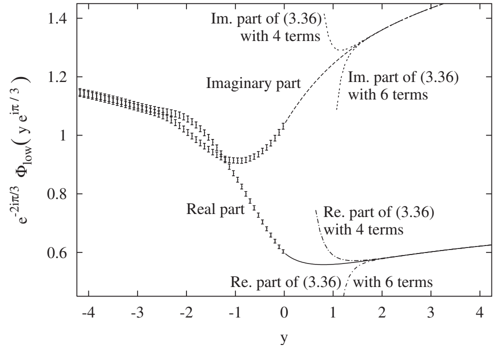

Fig. 14. The scaling function $\Phi_{\text{low}}(\eta)$ along the axis $\eta = ye^{\frac{i\pi}{3}}$ obtained through numerical analytic continuation (Section 8.2.1). Real and imaginary parts of $e^{-\frac{2\pi i}{3}}\Phi_{\text{low}}(ye^{\frac{i\pi}{3}})$ are shown. The $y<0$ part of this axis lays inside the shadow domain SHD in Fig. 4, close to the axis OA. The data here is not very accurate. Nevertheless, an anomaly around $y \simeq -2.5$ (presumably associated with the proximity of the YL singular point) seems to be developing.

example (which will turn out to be usefull in our analysis in Section 8.3) we show in Fig. 14 the shape of the function $\Phi_{\text{low}}(\eta)$ along the ray $\eta = ye^{i\frac{\pi}{3}}$, $y>0$, computed this way. Any changes induced by changing the cutoff procedure are by far too small ($<10^{-4}$) to be visible in this plot.

More interestingly, one can apply the relation

$$D_{\text{meta}}(y) = -\int_{-\infty}^{\infty} y^{-\frac{13}{16}-i\omega}\cosh(8\pi\omega/15)\,\Psi(\omega)\,\frac{d\omega}{2\pi} \tag{8.8}$$

(which is equivalent to the dispersion relation (3.15)) to compute the function (3.46). As expected, the resulting inverse Fourier transform (8.8) shows rapid decay at large y (see Fig. 15a). However, instead of monotonous decay (3.49), the cutoff integral (8.7) exhibits small oscillations whose shape is very sensitive to the details of the cutoff procedure. Therefore, we consider the results for the function $D_{\text{meta}}(y)$ obtained this way only reliable for $y<2.0$. To see how these results comply with the expected asymptotic form (5.9) we have plotted in Fig. 15b the ratio $D_{\text{meta}}(y)/V(y)$, where $V(y)$ is the exponent (3.50). The error bars in this plot represent the spread of the data obtained with different cutoff procedures. From (5.9), this ratio is expected to approach the constant 0.2161... as $y\to\infty$. As is seen from the plot, the ratio reaches a minimum ≈ 0.153 at $y\approx 1.15$, and then shows a tendency to increase towards the expected value.

Unfortunately, as was explained above, for $y>1.9$ the data obtained by this method becomes unreliable, and presently neither the true large y asymptotic nor the way it is approached can be established on their basis.

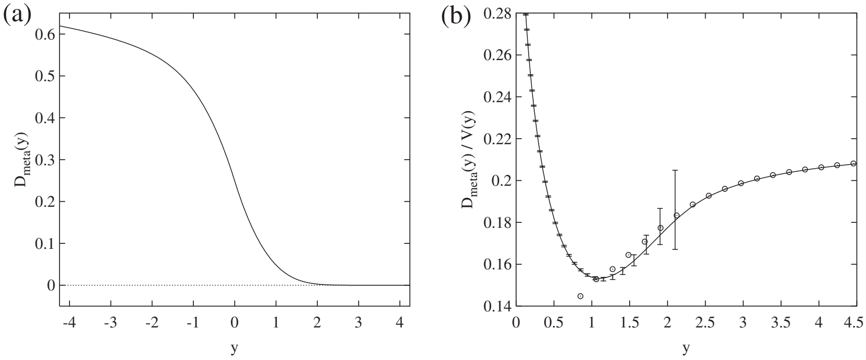

Fig. 15. (a) The function $D_{\mathrm{meta}}(y)$, Eq. (3.46), obtained through numerical analytic continuation in Section 8.2.1. (b) The ratio $D_{\mathrm{meta}}(y)/V(y)$ (where $V(y)$ is defined in Eq. (3.50)). The data from numerical analytic continuation (Section 8.2.1) (shown as error bars) *vs.* the data from resonance width analysis (Section 7.3) (shown as empty bullets). The solid curve is the plot of Eq. (8.14).

But fortunately, the analysis of Section 7.3 apparently provides a complimentary set of data. We replot in Fig. 15b the data from the resonance width analysis (identical to those in Fig. 13) to demonstrate its agreement with the data obtained by the Fourier analysis.

In principle, one could try to use this numerical Fourier transform $\Psi(\omega)$ to continue further, into the shadow domain, by taking $|\alpha| > 8\pi/15$ in (8.7). We found that while for $|\alpha| < 3\pi/5$ the intergal in (8.7) still receives dominating contribution from ω well within the window $|\omega| < \omega_{\max}$ (and hence is not too sensitive to the cutoff procedure), for larger α the domain around $\omega_{\max}$ becomes more significant. The result of such computation with $\alpha = -2\pi/3$ is shown in the left-hand side of Fig. 14; its accuracy is hardly better then 10^{-2}, and may be worse. For $|\alpha| > 2\pi/3$ the results are too sensitive to the cutoff procedure to be taken seriously. In other words, at present the accuracy of our direct data about $\Phi_{\mathrm{low}}(\eta)$ is not sufficient to support (or unvalidate) analyticity of this function in the whole of the shadow domain. In Section 8.3 later we use another approach, based on the extended dispersion relation, Eq. (4.8), to verify the extended analyticity.

8.2.2. Low-T Dispersion Relation

According to (3.15), in the low-T wedge $-8\pi/15 < \arg(\eta) < 8\pi/15$ (the domain LTW in Fig. 4) the scaling function $\Phi(\eta)$ is represented in terms of the function $D_{\mathrm{meta}}(y)$ as

$$\Phi(\eta) = \tilde{G}_1 \eta^{\frac{1}{8}} - \frac{15\eta^{-\frac{7}{4}}}{8\pi} \int_0^\infty \frac{D_{\mathrm{meta}}(y)\, y^{-\frac{9}{8}}\, dy}{y^{-\frac{15}{8}} + \eta^{-\frac{15}{8}}}. \tag{8.9}$$

It is interesting to check how the above information about $D_{\mathrm{meta}}(y)$ agrees with our direct data on this scaling function. Inspection of the plot in Fig. 15b shows that the function $D_{\mathrm{meta}}(y)$ is well approximated by the first eight terms of its power series expansion (3.47), i.e., by the polynomial

$$D_{\mathrm{meta}}^{<}(y) = D_0 + D_1\, y + \cdots + D_7 y^7, \tag{8.10}$$

whith the coefficients D_n computed from Φ_n's in Table III, all the way up to $y \approx 1.1$. This plot also shows that the above large-y approximation,

$$D_{\mathrm{meta}}^{>}(y) = (0.2161 - 0.136\, y^{-\frac{15}{8}})\, V(y), \tag{8.11}$$

seems to provide rather accurate approximation of this function for $y \gtrsim 2.5$. The two curves corresponding to (8.10) and (8.11) intersect at $y \approx 1.59$. We have checked that even if one just takes (8.10) and (8.11) as the approximations for $D_{\mathrm{meta}}(y)$ at $y < 1.59$ and $y > 1.59$ respectively, the dispersion integral (8.9) reproduces correctly at least four significant digits when compared with our direct data at real positive η. Of course such accuracy is related to the fact at $y \sim 1.59$ the function $D_{\mathrm{meta}}(y)$ is already rather small. In fact, much better approximation can be achieved if one uses some interpolation between (8.10) and (8.11) in the intermediate region. We have obtained very good results with the fifth-order polynomial interpolation

$$D_{\mathrm{meta}}^{\mathrm{interp}}(y) = [P_0 + P_1(y - y_1) + \cdots + P_5\,(y - y_1)^5]\, V(y), \tag{8.12}$$

with $y_1 = 1.1$ and the coefficients $P_0, \ldots, P_5$ fixed by the conditions that (8.12) matches smoothly (up to the second derivative) the approximations (8.10) and (8.11) at $y = 1.1$ and at $y = 2.72$, respectively,

$$\begin{aligned} P_0 &= 0.1532863, & P_1 &= 0.0002611, & P_2 &= 0.0499557, \\ P_3 &= -0.0209331, & P_4 &= -0.004408, & P_5 &= 0.002672. \end{aligned} \tag{8.13}$$

The dispersion integral (8.9) with

$$D_{\mathrm{meta}}(y) = \begin{cases} D_{\mathrm{meta}}^{<}(y) & \text{for } \ 0 < y < 1.1 \\ D_{\mathrm{meta}}^{\mathrm{interp}}(y) & \text{for } \ 1.1 < y < 2.72 \\ D_{\mathrm{meta}}^{>}(y) & \text{for } \ 2.72 < y < \infty \end{cases} \tag{8.14}$$

reproduces our direct data very accurately (with six significant digits, i.e., essentially within the estimated accuracy of the direct data), as is demonstrated in Table IV. In this computation we have used the exact value

(3.12) of the coefficient $\tilde{G}_1$ in (8.9), and again the value (7.1) of Y_0 was assumed.

The approximation (8.14) can be also used to estimate the coefficients $\tilde{G}_n$ of the assymptotic expansion (3.11). It follows from (3.13) that

$$\tilde{G}_n = (-)^{n+1} \frac{15}{8\pi} \int_0^\infty D(y)\, y^{\frac{(15n-24)}{8}}\, dy \qquad \text{for} \quad n > 1. \tag{8.15}$$

Moreover, the coefficient $\tilde{G}_1$ itself must coinside with the integral

$$\tilde{G}_1 = \frac{15}{8\pi} \int_0^\infty (D_{\text{meta}}(y) - D_0)\, y^{-\frac{9}{8}}\, dy, \tag{8.16}$$

lest analyticity of $\tilde{\Phi}(\eta)$ at $\eta = 0$ be violated. With our approximation (8.14) the integral (8.16) reproduces the coefficient $\tilde{G}_1$ almost exactly (if fact, we have used this as a condition in choosing the interpolation interval in (8.14)), and few higher coefficients obtained through (8.15) are compaired with previous estimates in Table II.

8.3. Extended Dispersion Relation

Equipped with the results in Sections 8.1 and 8.2, we made a preliminary analysis of analyticity in the shadow domain in order to validate the extended analyticity conjecture formulated in Section 4. If one assumes the extended analyticity, the estimates in Sections 8.1 and 8.2 make it possible to actually reconstruct, with reasonable precision, the behaviour of the function $\Phi(\eta)$ along the shadow side of the Yang–Lee branch cut in Fig. 4, thus finding an approximation for the discontinuity function

$$\Delta(y) = i\Phi_{\text{imh}}(-y) - ie^{-i\frac{8}{15}\pi}\Phi_{\text{low}}(ye^{-i\frac{11}{15}\pi}) \tag{8.17}$$

which enters the extended dispersion relation (4.8); the expression (8.17) is a simple consequence of (4.3) and (4.1). The extended analyticity is then verified by checking this dispersion relation against direct data.

Let us note that, on one hand, the results of Section 8.2 allow one to find the large-y asymptotic form of the function $\Phi_{\text{low}}(ye^{-i\frac{11}{15}\pi})$. Indeed, the second (analytic) form of the Eq. (3.46) which defines $D_{\text{meta}}(y)$ also defines its analytic continuation to complex values of its argument. The extended analyticity is equivalent to the statement that $D_{\text{meta}}(z)$ is analytic in the wedge $-\pi/5 < \arg(z) < \pi/5$. Under this assumption, it follows from (3.46) that

$$\Phi_{\text{low}}(ye^{-i\frac{11}{15}\pi}) = e^{-i\frac{32}{15}\pi}\Phi_{\text{low}}(ye^{\frac{i\pi}{3}}) + 2ie^{-i\frac{16}{15}\pi}\, D_{\text{meta}}(ye^{-\frac{i\pi}{5}}). \tag{8.18}$$

For real positive y, this equation expresses the desired values of $\Phi_{\text{low}}(\eta)$ on the shadow side of the branch cut in terms of its values well inside the domain LTW in Fig. 4, and also through the analytic continuation of the function $D_{\text{meta}}(y)$. The first term is already under good analytic control, see Section 8.2.1. In fact, for sufficiently large y the function $\Phi_{\text{low}}(y\, e^{\frac{i\pi}{3}})$ is approximated very well by first few terms of its asymptotic expansion (3.36), as illustrated in Fig. 14. Specifically, for $y > 3.0$ the first twelve terms of this expansion yield an accuracy better than $\sim 10^{-4}$. On the other hand, the large-y behaviour of the second term in (8.18) follows from the asymptotic law (5.9). With this, Eq. (8.18) yields approximation for the second term in Eq. (8.17), valid at sufficiently large y. This readily translates into corresponding large-y approximation for the function $\Delta(y)$, since the large-y behaviour of the first term in (8.17) follows from (3.38b) and (3.1). Finaly, one can check that for $y > 3$ the accuracy of at least $\sim 10^{-4}$ can be achieved by taking the first six terms (i.e., including G_{12} term) of the expansion (3.1). Therefore the following formula

$$\Delta(y) \approx \Delta^{>}(y) = \sum_{k=1}^{12} e^{-\frac{i\pi(k-1)}{2}} \left(G_k - e^{-\frac{i\pi k}{8}} \tilde{G}_k\right) y^{\frac{16-15k}{8}}$$

$$+2\left(V_0 + V_1 e^{\frac{3\pi i}{8}} y^{-\frac{15}{8}}\right) y^{\frac{1}{8}} \exp\left\{ -\mu e^{-\frac{3\pi i}{8}} y^{\frac{15}{8}} + \frac{3\pi i}{8} \right\} \tag{8.19}$$

is expected to approximate the discontinuity function well for sufficiently large y. In (8.19) μ stands for $\pi/2\bar{s}$, and it is understood that $G_{2n+1} = 0$.

On the other hand, when y is close to Y_0 the relation (4.2) is usefull. The approximation (8.3) for $D_{\text{imh}}(y)$ then suggests the following approximation

$$\Delta(y) \approx \Delta^{<}(y) = y^2/4 - \theta(y - Y_0) \left(\frac{1}{2}\, \bar{B}_0 e^{-i\frac{5\pi}{6}} (y - Y_0)^{\frac{5}{6}} + \frac{1}{2}\, \bar{B}_1 e^{-i\frac{5\pi}{6}} (y - Y_0)^{\frac{11}{6}} \right.$$

$$\left. - \frac{\sqrt{3}}{2}\, \bar{C}_0 e^{-i\frac{5\pi}{3}} (y - Y_0)^{\frac{5}{3}} \right), \tag{8.20}$$

which is expected to be valid at $y \simeq Y_0$. In (8.20) $\theta(x)$ is the step function.

The plots of (8.19) and (8.20) are shown in Fig. 16. In this plot the numerical values (8.4) of the coefficients in (8.20) are taken. Also, the coefficients V_0 and V_1 in (8.19) are identical to those in (8.11), and the coefficients G_k and $\tilde{G}_k$ are taken from the Tables I and II. In fact, contributions of the terms with $k > 5$ in the sum in (8.19), as well as the differences in the choice between the columns in that tables, are too small to be visible in this plots. One can see that the approximations (8.19) and (8.20) match each other very well in the intermediate region of y around 3. This match itself can be viewed as a support to the extended analyticity conjecture. Even more convincing result is obtained by evaluating the extended dispersion relation (4.8) with the use of these approximations. We have evaluated the integral (4.8) with

$$\Delta(y) = \begin{cases} \Delta^{<}(y) & \text{for} \quad 0 < y < 3 \\ \Delta^{>}(y) & \text{for} \quad 3 < y \end{cases} \tag{8.21}$$

for some real values of η. In this calculation specific numerical values of the coefficients G_{2n} from the second column in Table I and $\tilde{G}_k$ from the second column in Table II, as well as the values (8.11) of V_0, V_1, were used. The results for the function $\Phi(\eta)$ are compared to our direct data in Table IV. Also, the first coefficients Φ_n obtained through (4.10), within the same approximation, are presented in Table III. Although the agreement is not very accurate (the values of $\Phi(\eta)$ agree with the direct data with only four digits, which is well below the estimated accuracy of the latter), we take it as a strong support of extended analyticity. The relatively low accuracy should probably be attributed to low quality of the approximation (8.20); we believe it would improve when better estimates of the coefficients in (3.41b)–(3.41c) are obtained, and higher subleading singular terms in (3.40) are included.

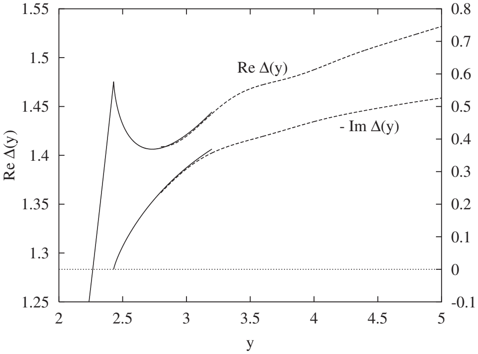

Fig. 16. Plots of real and imaginary parts of $\Delta^{<}(y)$, Eq. (8.20) (shown as solid lines), and $\Delta^{>}(y)$, Eq. (8.19) (dashed lines).

9. DISCUSSION

In this work we have used numerical data obtained by TFFSA to study the scaling function $\Phi(\eta)$ associated with the Ising model free energy in its critical domain. We estimated some parameters of this function, including location of the Yang–Lee singularity (7.1) and leading amplitudes (7.2a), (7.2b) of associated singular expansion (3.40). We also examined the analyticity of the scaling function. Our analysis confirmed the standard analyticity assumption (see Section 3), and we have found strong evidence in support of the "extended analyticity" conjectured in Section 4. Here we would like to explain why we regard proving (or invalidating) this extended analyticity as an important issue.

As is known, in the classical theory of phase transitions, which does not incorporate fluctuational effects, the Langer's singularity of the low-T free energy at $H=0$ is not present. Instead, analytic continuation of the classical low-T free energy shows a branch-cut singularity at some finite negative value of H, $H=-H_{\mathrm{SP}}$, known as the "spinodal point." This singularity appears because at sufficiently large H ($|H|>H_{\mathrm{SP}}$) the metastable state becomes unstable against classical decay. When fluctuations are taken into account the free energy becomes singular (albeit weakly singular) at $H=0$, since the metastable phase is always prone to decay through nucleation. But what happens to the spinodal singularity? There are convincing arguments (see ref. 50) to that in the presence of fluctuations the (analytic continuation of the) free energy cannot have singularities at real negative H. In our opinion, the most plausible possibility is that in fluctuational theory the spinodal singularity does not just disappear but instead gets pushed under the Langer's branch cut, as is shown schematicaly in Fig. 2. In other words, the nearest singularity under the Langer's branch cut could be associated with the "ideal limit of metastability,"[51] where a transition from a decay through nucleation to faster "classical" mechanism of decay takes place. The transition can be more or less expressed depending on how far under the cut the singularity is located. The above speculation is made under assumption that the analytic continuation of the free energy is a quantity at all relevant to thermodynamics of the metastable state, even away from the domain of vanishingly small H. It also ignores all possible kinetic aspects of the problem, certainly important in realistic situations. Nontheless, it was one of the motivations for the presented study of analyticity under the branch cut in Fig. 2. The "extended analyticity" proposed in Section 4 is the statement that the nearest singularity under this branch cut is identical to the Yang–Lee singularity in Fig. 1. In these terms, the "true spinodal" is the Yang–Lee singularity (viewed from the shadow side, as in Fig. 4).

Our analysis concerned explicitly with the $D=2$ system. In this case the Yang–Lee singularity turns out to be located relatively far under the branch cut. The phase of ξ_{SP} in Fig. 2 (which is related to the angular size of the "shadow domain" in Fig. 4) is $3\pi/8$. However, on a formal level, it is not difficult to extend the analysis of Section 3 to any $1<D<4$. In this generic case the angular size θ of analogous shadow domain can be expressed in terms of the standard Ising model critical exponents as

$$\theta=\pi-\frac{3\pi}{2}\frac{1}{2-\alpha-\beta}. \tag{9.1}$$

It follows from what we know about the D-dependence of the Ising critical exponents (see, e.g., ref. 52) that when D increases from 2 to 4 the angular size of the "shadow domain" decreases, and goes to zero as the critical exponents approach their classical values at $D=4$. A simple estimate shows that at $D=3$ this angular size is $\approx 0.04\pi$. If similar "extended analyticity" assumption could be validated in this case, one should expect the effect of the Yang–Lee singularity being quite prominent at real negative H, at least in the critical domain $T\to T_c$. Unfortunately, at the moment we do not see any practical way to check this assumption away from the $D=2$ case.

Even in the $D=2$ case many issues call for refinement. First, although the extended dispersion relation did check in Section 8 rather convincingly with present data about the discontinuity (8.17), the agreement in Table IV is not too precise, and hence very weak singularities in the shadow domain are not excluded. Much better knowledge about the "fine-structure" of the Yang–Lee singularity (in particular, better estimates of the coefficients of the expansions (3.41b), (3.41c)) would be usefull in order to establish the extended analyticity "beyond any reasonable doubt." We hope to make progress in this direction in the future. We also want to stress here that even that would not settle the question of analytic properties of the scaling function completely. What one should expect when going under the Yang–Lee branch cut in Fig. 4 from the shadow domain? This and related questions require at least some understanding of the physics governing the "shadowy side" of the Yang–Lee edge singularity.

Let us also mention some possible further developments, not related directly to the free energy, which we hope to address in the future:

(i) Analytic properties of the correlation length (defined as inverse mass M_1), can be studied along the same lines. We expect associated scaling function to enjoy similar extended analyticity.

(ii) Detailed quantitative study of the IFT (1.1), viewed as the particle theory, is possible using TFFSA. This is a beautifull model of quark confinement, simple but rich in phenomena.[(48)]

(iii) Physical interpretation of the IFT with pure imaginary h is a particularly intriguing question. Even the qualitative pattern of the higher finite-size energy levels $E_i(R)$ in this case is yet to be understood.

We would like to stress here that in this work we are concerned only with the leading singular term $\mathscr{F}_{\text{sing}}(T, H)$ of the Ising free energy, which is governed by the field theory (1.1). Subleading singular terms appearing in the lattice Ising model, and convergence of associated singular expansion, are important separate questions which are not addressed here. Possible subtleties in such expansion are discussed in interesting recent papers.[(53–55)]

APPENDIX A

Here we present a simple derivation of the finite-size matrix elements (2.12) using the symmetries of the "doubled" Ising field theory with $h = 0$. This derivation is one of the results of ref. 56, where these symmetries are exploited to a greater extent (in particular, the nonlinear differential equations of ref. 8 are shown to be a consequence of these symmetries).

Consider two copies of the free-fermion system (2.2). We will use the subscripts a and b to distinguish between the fields corresponding to these copies. Thus, $(\psi_a, \bar{\psi}_a)$ and $(\psi_b, \bar{\psi}_b)$ will stand for the two species of Majorana fermi fields, σ_a and σ_b will denote the associated spin fields, etc. We will also use the notations $a^\dagger$, a and $b^\dagger$, b for the fermion creation and anihilation operators associated with the two copies; these operators are assumed to satisfy the canonical anticommutators (2.6) between themselves, and $a^\dagger$, a anticommute with $b^\dagger$, b. Of course, this doubled Majorana fermion system is equivalent to a single copy of a free Dirac fermion.

We will study this system in a finite-size geometry, with the spatial coordinate x compactified on a circle of circumference R. Let us call $\mathscr{H}_{\text{diag}}$ the space of states generated by the creation operators $a^\dagger$, $b^\dagger$ from the "diagonal" vacua $|0\rangle_{\text{NS, NS}} \equiv |0\rangle_{\text{NS}, a} \otimes |0\rangle_{\text{NS}, b}$ and $|0\rangle_{\text{R, R}} \equiv |0\rangle_{\text{R}, a} \otimes |0\rangle_{\text{R}, b}$. Consider the operator

$$\mathbf{Y} = \frac{1}{2\pi} \int_0^R \left[\psi_a \partial \psi_b + \frac{im}{2} \bar{\psi}_a \psi_b \right] d\mathrm{x} \tag{A.1}$$

acting in the space $\mathscr{H}_{\text{diag}}$. It is easy to check that it commutes with the Hamiltonian of this doubled system, and anihilates both the above "diagonal" vacua $|0\rangle_{\text{NS, NS}}$ and $|0\rangle_{\text{R, R}}$. This operator is just one of the generators of the infinite-dimensional algebra $\widehat{SL(2)}$ of the local integrals of motion of the free Dirac field theory;(57) in fact, for our present limited purpose no knowledge about the other generators is needed. It is straightforward to derive the commutators

$$[\mathbf{Y}, \mu_a(x)\, \mu_b(x)] = \sigma_a(x)\, \partial\sigma_b(x) - \partial\sigma_a(x)\, \sigma_b(x), \tag{A.2a}$$

$$[\mathbf{Y}, \sigma_a(x)\, \mu_b(x)] = -i\, (\mu_a(x)\, \partial\sigma_b(x) - \partial\mu_a(x)\, \sigma_b(x)), \tag{A.2b}$$

where again ∂ stands for $\frac{1}{2}(\partial_{\mathrm{x}} - i\partial_{\mathrm{y}})$, and $\mu(x)$ are the dual spin field.(25) It is also straightforward to compute the action of this operator on arbitrary states containing a and b particles. For instance, for the excitations over the vacuum $|0\rangle_{\mathrm{R,R}}$ one obtains

$$\mathbf{Y} = \sum_{n\in\mathbb{Z}} \frac{m}{2}\, e^{\theta_n}[a_n^\dagger b_n + b_n^\dagger a_n], \tag{A.3}$$

where θ_n are defined in (2.13). Similar expression (with $n \to k \in \mathbb{Z}+\frac{1}{2}$) holds for the action of $\mathbf{Y}$ in the NS-NS sector. We are going to show that the general structure of the matrix elements (2.12) (with the exception of the explicit expressions (2.19) for the "leg factors" g and $\tilde{g}$, which will be derived in the second part of this section) is a simple consequence of the relations (A.2) and (A.3).

To save on writing, we will restrict attention to the case $m > 0$, and explicitly derive only the particular case $K = 0$ of the expression (2.12); the analysis can be extended to a other cases in a straightforward way. We will use the notations

$$M_{0,N}(n_1,..., n_N) = \begin{Bmatrix} {}_{\mathrm{NS}}\langle 0|\, \sigma(0,0)\, |n_1,..., n_N\rangle_{\mathrm{R}} & \text{for even } N \\ {}_{\mathrm{NS}}\langle 0|\, \mu(0,0)\, |n_1,..., n_N\rangle_{\mathrm{R}} & \text{for odd } N \end{Bmatrix} \tag{A.4}$$

If N is even, take the identity

$$0 = {}_{\mathrm{NS,NS}}\langle 0|\, \mathbf{Y}, \mu_a(x)\, \mu_b(x)\, a_{n_1}^\dagger \cdots a_{n_N}^\dagger\, |0\rangle_{\mathrm{R,R}}. \tag{A.5}$$

which follows from ${}_{\mathrm{NS,NS}}\langle 0|\, \mathbf{Y} = 0$. If N is odd, similar identity, with $\mu_a(x)\, \mu_b(x)$ replaced by $\sigma_a(x)\, \mu_b(x)$, should be used. The matrix element in the r.h.s. of (A.5) can be written as a sum of the matrix element of the commutator (A.2a) and the matrix element of $\mu_a(x)\, \mu_b(x)\, \mathbf{Y}$. Using (A.3) to compute the latter, one obtains the relation

$$M_{0,0}\, M_{0,N}(n_1,..., n_N) \sum_{j=1}^{N} (e^{\theta_{n_j}})$$
$$= I \sum_{j=1}^{N} (-1)^{j-1}\, e^{\theta_{n_j}}\, M_{0,1}(n_j)\, M_{0,N-1}(n_1,..., n_{j-1}, n_{j+1},..., n_N), \tag{A.6}$$

where $I = i$ if N is even, and $I = 1$ if N is odd. This relation allows one to obtain recurrently all the matrix elements (A.4) in terms of $M_{0,0}$ and $M_{0,1}(n)$. It is not difficult to show that the solution of this recurrent relation has the form

$$M_{0,N}(n_1,..., n_N) = i^{[N/2]}\, M_{0,0} \left(\prod_{i=1}^{N} g(\theta_{n_i}) \right) f_N(\theta_{n_1},..., \theta_{n_N}), \tag{A.7}$$

where $[N/2]$ denotes the integer part of $N/2$,

$$g(\theta_n) \equiv M_{0,1}(n)/M_{0,0}, \tag{A.8}$$

and

$$f_N(\theta_1,..., \theta_N) = \prod_{i<j}^{N} \tanh\left(\frac{\theta_{n_i} - \theta_{n_j}}{2}\right). \tag{A.9}$$

This follows from the well known identities$^{(58)}$ that the products (A.9) obey,

$$\begin{aligned} & f_{0,N+1}(\theta, \theta_1,..., \theta_N) \\ & \quad = \sum_{j=1}^{N} (-)^{j-1} \tanh\left(\frac{\theta - \theta_j}{2}\right) f_{0,N-1}(\theta_1,..., \theta_{j-1}, \theta_{j+1},..., \theta_N) \end{aligned} \tag{A.10}$$

If one expands (A.10) around $\theta = +\infty$, the term $\sim e^{-\theta}$ yields exactly (A.6).

It remains to determine the factors $M_{0,0}$ and $g(\theta)$ in (A.7). The first is known from ref. 26, see Eqs. (2.16)–(2.17). To find the factors $g(\theta_n) = {}_{\mathrm{NS}}\langle 0|\, \mu(0)\, |n\rangle_{\mathrm{R}} / {}_{\mathrm{NS}}\langle 0|\, \sigma(0)\, |0\rangle_{\mathrm{R}}$, let us return to the single Majorana fermion system (2.2), and consider the matrix element

$$\Psi(\mathrm{x}, \mathrm{y}) = {}_{\mathrm{NS}}\langle 0|\, \mu(0,0)\, \psi(\mathrm{x}, \mathrm{y})\, |0\rangle_{\mathrm{R}} / {}_{\mathrm{NS}}\langle 0|\, \sigma(0,0)\, |0\rangle_{\mathrm{R}}, \tag{A.11}$$

and similar matrix element $\bar{\Psi}(\mathrm{x}, \mathrm{y})$ defined as in Eq. (A.11) with $\psi(\mathrm{x}, \mathrm{y})$ replaced by $\bar{\psi}(\mathrm{x}, \mathrm{y})$. Here x, y are the cartesian coordinates on the euclidean space-time cilinder, x being the periodic direction. The functions Ψ and $\bar{\Psi}$ have the following properties:

(i) They satisfy the Majorana field equations

$$\bar{\partial}\Psi(\mathrm{x}, \mathrm{y}) = \frac{im}{2}\, \bar{\Psi}(\mathrm{x}, \mathrm{y}), \qquad \partial\bar{\Psi}(\mathrm{x}, \mathrm{y}) = -\frac{im}{2}\, \Psi(\mathrm{x}, \mathrm{y}); \tag{A.12}$$

(ii) $\Psi(\mathrm{x}, \mathrm{y})$ is an analytic function for all real x, y except at the points $(\mathrm{x}, \mathrm{y}) = (0 (\mathrm{mod}\, R), 0)$, and it obeys the (anti)periodicity conditions

$$\Psi(\mathrm{x}+R, \mathrm{y}) = \left\{ \begin{array}{ll} \Psi(\mathrm{x}, \mathrm{y}) & \text{for } \mathrm{y} < 0 \\ -\Psi(\mathrm{x}, \mathrm{y}) & \text{for } \mathrm{y} > 0 \end{array} \right\}. \tag{A.13}$$

The function $\bar{\Psi}$ obeys the same conditions.

(iii) Their singularities at $(\mathrm{x}, \mathrm{y}) = (0, 0)$ are such that

$$\lim_{\mathrm{x}, \mathrm{y} \to 0} \sqrt{2\, z}\, \Psi(\mathrm{x}, \mathrm{y}) = e^{-\frac{i\pi}{4}}, \qquad \lim_{\mathrm{x}, \mathrm{y} \to 0} \sqrt{2\bar{z}}\, \bar{\Psi}(\mathrm{x}, \mathrm{y}) = e^{\frac{i\pi}{4}}, \tag{A.14}$$

where $z = \mathrm{x} + i\mathrm{y}$, $\bar{z} = \mathrm{x} - i\mathrm{y}$. Also, the functions $\Psi(\mathrm{x}, \mathrm{y})$ and $\bar{\Psi}(\mathrm{x}, \mathrm{y})$ are bounded when $|\mathrm{y}| \to \infty$.

It is possible to show that the above conditions (i)–(iii) define the functions uniquely. The solution to these conditions has the form

$$\Psi(\mathrm{x}, \mathrm{y}) = \sum_{n \in \mathbb{Z}} \sqrt{\frac{\pi}{R \cosh \theta_n}}\, e^{\frac{\theta_n}{2}}\, g(\theta_n)\, e^{m\mathrm{y} \cosh \theta_n - im\mathrm{x} \sinh \theta_n}, \quad \text{for } \mathrm{y} < 0, \tag{A.15a}$$

$$\Psi(\mathrm{x}, \mathrm{y}) = -i \sum_{k \in \mathbb{Z} + \frac{1}{2}} \sqrt{\frac{\pi}{R \cosh \theta_k}}\, e^{\frac{\theta_k}{2}}\, \tilde{g}(\theta_k)\, e^{-m\mathrm{y} \cosh \theta_k + im\mathrm{x} \sinh \theta_k}, \quad \text{for } \mathrm{y} > 0, \tag{A.15b}$$

where θ_n and θ_k are the solutions of the Eqs. (2.13), and the functions $g(\theta)$ and $\tilde{g}(\theta)$ are defined through the integrals (2.18). The function $\bar{\Psi}(\mathrm{x}, \mathrm{y})$ is given by the same sums (A.15a), (A.15b), but with the factor $e^{\frac{\theta}{2}}$ replaced by $e^{-\frac{\theta}{2}}$. It is clear that the sums (A.15a), (A.15b) satisfy (A.12)–(A.14), and one only needs to check that the analytic continuation of (A.15a) to $\mathrm{y} > 0$ coincides with (A.15b), and vice versa. This is done using standard tricks with contour deformations. One can write (A.15a), (A.15b) in terms of the contour integrals

$$\Psi(\mathrm{x}, \mathrm{y}) = \sqrt{\pi m} \int_{\mathscr{C}_- + \mathscr{C}_+} \frac{d\theta}{2\pi} \frac{G(\theta)\, e^{\frac{\theta}{2}}}{1 - e^{-imR \sinh \theta}}\, e^{m\mathrm{y} \cosh \theta - im\mathrm{x} \sinh \theta} \quad \text{for } \mathrm{y} < 0, \tag{A.16a}$$

$$\Psi(\mathrm{x}, \mathrm{y}) = i \sqrt{\pi m} \int_{\mathscr{C}_- + \mathscr{C}_+} \frac{d\theta}{2\pi} \frac{G(\theta)^{-1}\, e^{\frac{\theta}{2}}}{1 + e^{imR \sinh \theta}}\, e^{-m\mathrm{y} \cosh \theta + im\mathrm{x} \sinh \theta} \quad \text{for } \mathrm{y} > 0, \tag{A.16b}$$

where $G(\theta) = \exp(\kappa(\theta))$, with $\kappa(\theta)$ defined as the integral (2.19), $G(\theta)^{-1}$ stands for $1/G(\theta)$ (not for the inverse function), and the integration is performed along the contours $\mathscr{C}_-$, which runs from $-\infty$ to $+\infty$ just below the real axis, and $\mathscr{C}_+$, which returns back to $-\infty$ just above the real axis. The function $G(\theta)$ is meromorphic, and both $G(\theta)$ and $G(\theta)^{-1}$ are analytic in the strip $-\pi < \Im m\, \theta < \pi$. It is easy to verify that

$$G(\theta+i\pi/2)\, G(\theta-i\pi/2) = \frac{e^{mR\cosh\theta}-1}{e^{mR\cosh\theta}+1}. \tag{A.17}$$

If, for instance, $0 < \mathrm{x} < R$, then the contour $\mathscr{C}_-$ in (A.16a) and (A.16b) can be shifted downward, $\theta \to \theta - i\pi/2$, while the contour $\mathscr{C}_+$ admits upward shift $\theta \to \theta + i\pi/2$. After this deformation the integral (A.16a) assumes the form

$$\begin{aligned}\Psi(\mathrm{x},\mathrm{y}) = \sqrt{\pi m}\int_{-\infty}^{\infty}\frac{d\theta}{2\pi}\Bigg[&\frac{G(\theta-i\pi/2)\, e^{\frac{\theta}{2}-i\frac{\pi}{4}}}{1-e^{-mR\cosh\theta}}\, e^{-im\mathrm{y}\sinh\theta - m\mathrm{x}\cosh\theta}\\ &-\frac{G(\theta+i\pi/2)\, e^{\frac{\theta}{2}+i\frac{\pi}{4}}}{1-e^{mR\cosh\theta}}\, e^{im\mathrm{y}\sinh\theta + m\mathrm{x}\cosh\theta}\Bigg]\end{aligned} \tag{A.18}$$

As long as x remains within the above interval, this integral now converges at all y, both negative and positive; it thus defines the analytic continuation of (A.16a) to all y. The same contour deformations applied to (A.16b) yields the integral which coincides with (A.18) in virtue of (A.17).

In fact, it is not difficult to find in a similar way a complete basis of functions $\Psi(\mathrm{x},\mathrm{y})$ which satisfy (A.12)—(A.14), but are allowed to grow at $|\mathrm{y}| \to \infty$; this basis then can be used to derive the full set of matrix elements (2.12) directly. We will discuss this topic in greater detail elsewhere.

APPENDIX B

In this section we describe some properties of the energy spectrum of the Hamiltonian (2.3) in the low-T domain $m > 0$. In subsection BI below we warm up with the derivation of the small h expansion (5.2) of the meson masses, and in BII we discuss the relation of the near-intersection pattern in Fig. 6a to the characteristics of the "false vacuum" resonance.

BI. As is well known, in the low-T regime the interaction term $h\int \sigma(x)\, d^2x$ in (2.1) gives rise to a confining interaction between the fermions of (2.2) (the "quarks"). As the result, the particle spectrum of the IFT (1.1) with $h \neq 0$ consists of bound states of the quarks—the "mesons." If h is sufficiently small, the lower part of the meson spectrum can be studied within the two-quark approximation. One looks for the meson state (in its rest frame) in the form

$$|\Psi\rangle = \frac{1}{2}\int_{-\infty}^{\infty} \frac{dp}{2\pi}\, \tilde{\Psi}(p)\, a_p^\dagger a_{-p}^\dagger\, |0\rangle, \tag{B.1}$$

and ignores all multiquark components. Here $a_p^\dagger$ are the quark creation operators normalized according to the canonical anticommutators $\{a_p, a_{p'}^\dagger\} = 2\pi\,\delta(p-p')$, and $\tilde{\Psi}(p)$ is the momentum-space wave function, which is assumed to be antisymmetric, i.e., $\tilde{\Psi}(p) = -\tilde{\Psi}(-p)$. Within this approximation the eigenvalue problem for the Hamiltonian (2.3) (with $R=\infty$) leads to the Bethe–Salpeter equation

$$\begin{aligned}(2\omega(p)-E)\,\tilde{\Psi}(p) = \frac{t^3}{2} ⨍_{-\infty}^{\infty} \frac{m^2}{\omega(p)\,\omega(p')} \Bigg[\left(\frac{\omega(p)+\omega(p')}{p-p'}\right)^2 \\ + \frac{1}{2}\frac{pp'}{\omega(p)\,\omega(p')}\Bigg] \tilde{\Psi}(p')\,\frac{dp'}{2\pi},\end{aligned} \tag{B.2}$$

where the principal value of the integral in the right-hand side is understood, E stands for the meson's rest energy, and the notations $\omega(p) = \sqrt{m^2+p^2}$ and

$$t = \left(\frac{2\bar{\sigma}h}{m^2}\right)^{\frac{1}{3}} \equiv (2\bar{s}\xi)^{\frac{1}{3}} \tag{B.3}$$

are used. The easiest way to derive this equation is to use the finite-size matrix elements (2.12) with $N = M = 2$ and take the limit $R\to\infty$.

The two-particle approximation is justified if h is small and E is sufficiently close to $2m$. In this case one can consistently treat the momenta p, p' in (B.2) as small as compaired to m. Making a rescaling

$$p = (mt)\,k, \qquad p' = (mt)\,k', \tag{B.4}$$

and expanding the operators in (B2) in the powers of t, one has

$$\begin{aligned}&\left[-\epsilon + k^2 - \frac{t^2}{4}k^4 + \frac{t^4}{8}k^6 + \cdots\right]\tilde{\Psi}((mt)\,k) \\ &\quad = ⨍_{-\infty}^{\infty}\left[\frac{2}{(k-k')^2} + \frac{t^4}{8}(k+k')^2 + \cdots\right]\tilde{\Psi}((mt)\,k')\,\frac{dk'}{2\pi},\end{aligned} \tag{B.5}$$

where ϵ is defined as

$$E - 2m = (mt^2)\,\epsilon. \tag{B.6}$$

It is useful to write down the configuration-space form of the Eq. (B.5),

$$\left[-\epsilon+|X|-\frac{d^2}{dX^2}-\frac{t^2}{4}\frac{d^4}{dX^4}-\frac{t^4}{8}\frac{d^6}{dX^6}+\cdots\right]\psi(X)=\left[-\frac{t^4}{2}\,\delta'(X)+\cdots\right]\psi(X), \tag{B.7}$$

where the configuration-space wave function

$$\psi(X)=\int_{-\infty}^{\infty}\frac{dk}{2\pi}\,e^{ikX}\,\tilde{\Psi}((mt)\,k) \tag{B.8}$$

is written in terms of the rescaled coordinates,

$$X=(mt)(\mathrm{x}_1-\mathrm{x}_2), \tag{B.9}$$

x_1, x_2 being the positions of the quarks. This function also is antisymmetric,

$$\psi(X)=-\psi(-X). \tag{B.10}$$

In Eqs. (B.5) and (B.7) the omitted terms $\cdots$ are $\sim t^6$ or smaller.

In the leading order in t^2 the Eq. (B.7) is just the Schrödinger equation with the linear potential $|X|$. It leads to the assymptotic formula (5.1) for the meson masses (first obtained in ref. 48). One can calculate further corrections by solving (B.7) perturbatively in t^2. Let $A(X)$ be a solution of the Airy equation

$$\left[X-\frac{d^2}{dX^2}\right]A(X)=0. \tag{B.11}$$

It is straightforward to check that the function

$$\begin{aligned}F(X)=A(X)&-\frac{t^2}{20}\,[4X\,A(X)+X^2\,A'(X)]\\&+\frac{t^4}{4}\left[\left(-\frac{X^2}{7}+\frac{X^5}{200}\right)A(X)+\left(-\frac{11}{35}+\frac{X^3}{35}\right)A'(X)\right]+O(t^6)\end{aligned} \tag{B.12}$$

(where prime denotes the derivative) is the perturbative solution of the equation

$$\left[X-\frac{d^2}{dX^2}-\frac{t^2}{4}\frac{d^4}{dX^4}-\frac{t^4}{8}\frac{d^6}{dX^6}+O(t^6)\right]F(X)=0, \tag{B.13}$$

and that the function

$$\psi(X) = \mathrm{sign}(X)\, F(|X| - \epsilon) \tag{B.14}$$

solves (in the same perturbative sense) the equation (B.7), provided

$$F(-\epsilon) = O(t^2); \tag{B.15a}$$

$$F(-\epsilon) + \frac{t^2}{2} F''(-\epsilon) = O(t^4); \tag{B.15b}$$

$$F(-\epsilon) + \frac{t^2}{4} F''(-\epsilon) + \frac{t^4}{8} F''''(-\epsilon) - \frac{t^4}{4} F'(-\epsilon) = O(t^6). \tag{B.15c}$$

Now, let Ai(X) and Bi(X) be the two canonical solutions of the Airy equation (B.11), and $F_A(X)$ and $F_B(X)$—the associated perturbative solutions (B.12) of (B.13). A straightforward calculation shows that the linear combination

$$F(X) = F_A(X) + \sigma(\epsilon)\, F_B(X) \tag{B.16}$$

with

$$\sigma(\epsilon) = -\frac{\mathrm{Ai}(-\epsilon)}{\mathrm{Bi}(-\epsilon)} \Bigg[1 + \frac{t^2 \epsilon^2}{20} \left(\frac{\mathrm{Bi}'(-\epsilon)}{\mathrm{Bi}(-\epsilon)} - \frac{\mathrm{Ai}'(-\epsilon)}{\mathrm{Ai}(-\epsilon)} \right) - \frac{t^4}{20} \left(\frac{\mathrm{Bi}'(-\epsilon)}{\mathrm{Bi}(-\epsilon)} - \frac{\mathrm{Ai}'(-\epsilon)}{\mathrm{Ai}(-\epsilon)} \right) \left(\frac{2\epsilon^3}{35} - \frac{57}{14} - \frac{1}{20} \frac{\mathrm{Bi}'(-\epsilon)}{\mathrm{Bi}(-\epsilon)} \right) + O(t^6) \Bigg] \tag{B.17}$$

satisfies the conditions (B.15a)–(B.15c), i.e., (B.14) with this $F(X)$ solves (B.7).

In the bound-state problem one is interested in the normalizable solutions of (B.7), $\int_{-\infty}^{\infty} |\psi(X)|^2\, dX < \infty$, i.e.

$$\psi(X) \to 0 \qquad \text{as} \quad |X| \to \infty. \tag{B.18}$$

Therefore, the bound-state eigenvalues of the energy parameter ϵ in (B.7) coincide with the zeroes of the amplitude $\sigma(\epsilon)$ in (B.16). From (B.17) one finds for these zeroes,

$$\epsilon_i = z_i - \frac{t^2}{20} z_i^2 - \frac{t^4}{280} \left(57 - \frac{11}{5} z_i^3 \right) + O(t^6). \tag{B.19}$$

where $-z_i$, $i = 1, 2, 3, \ldots$, are the zeroes of the Airy function, $\mathrm{Ai}(-z_i) = 0$.

It is straightforward to continue this perturbative expansion to higher orders in t^2. However, without proper modifications this does not make much sense because, starting with the order t^4 in (B.7), this expansion exceeds the accuracy of the two-particle approximation. The exact meson state $|\Psi\rangle$ contains four-quark, six-quark, and higher components which are neglected in (B.1). One can check that these multi-quark components lead to certain corrections to the r.h.s. of (B.2) which start with the terms $\sim t^4$. Therefore, strictly speaking, even the terms $\sim t^4$ in (B.7) and in (B.19) go beyond the accuracy of the two-quark approximation. However, it is possible to argue that the whole of the leading ($\sim t^6$) correction to (B.2) due to the multi-quark contributions has the form of the quark mass renormalization (5.8), i.e., it ammounts to adding a momentum-independent term $t^4 Q_2/2$ to the l.h.s. of (B.7). In turn, this leads to the shift $\epsilon_i \to \epsilon_i + t^4 q_2/2$ in (B.19). Using (B.6) one arrives at the expansion (5.2).

BII. In the low-T domain $m > 0$ the ground state of the IFT with $R = \infty$ and $h = 0$ is two-fold degenerate, with the two vacuum states $|0\rangle_\pm$ corresponding to the oposite values of the spontaneous magnetization,

$$_\pm\langle 0|\,\sigma(x)\,|0\rangle_\pm = \pm\bar{\sigma}. \tag{B.20}$$

Adding the interaction term $h\int \sigma(x)\,d^2x$ with small positive h lowers the energy density associated with the state $|0\rangle_-$ and raises the energy density of $|0\rangle_+$. That is, the state $|0\rangle_-$ becomes the true vacuum of the perturbed system, while the state $|0\rangle_+$ looses its stability and becomes the "false vacuum"—the global resonance state with the complex energy (3.16).

If h is small, the "false vacuum" decay rate can be computed using the saddle-point analysis in the Euclidean space-time.[(39–41, 21)] This analysis suggests the following qualitative picture of the decay process in real time. The quantum mechanical tunneling process results in the simultaneous formation of two quarks separated by the distance $R_d = 2m/\Delta F \approx m/\bar{\sigma}h$, which then speed away from each other, the expanding region between the quarks being the nucleus of the true vacuum. The distance R_d is the size of the "critical droplet" in the droplet model calculation.[(20, 21)] As long as the separation $R_{1,2}$ between the quarks remains close to R_d, the state can be described in term of non-relativistic quantum mechanics of the two-quark system with the *repulsive* linear potential $-2h\bar{\sigma}\,R_{1,2}$. If $|R_{1,2} - R_d| \ll R_d$, a generic state of such two-quark system is described by the wave function

$$\psi(Y) \sim A_+(Y - \epsilon') + S_{\text{res}}(E)\,A_-(Y - \epsilon'), \tag{B.21}$$

where $Y=(mt)(R_d-R_{1,2})$ (the parameter t is defined in (B.3)), $(mt^2)\,\epsilon'=E-E_{\mathrm{res}}$ is suitably normalized energy of the system over the energy E_{res} of the "false vacuum," and $A_\pm$ are the solutions of the Airy equation (B.11),

$$A_\pm(Y)=\mathrm{Ai}(Y)\pm i\mathrm{Bi}(Y). \tag{B.22}$$

These are the "running wave" solutions, the wave $A_-(Y)$ being the state of the quarks speeding away from each other. The "scattering amplitude" S_{res} in (B.21) should be determined (in principle) by solving the problem in the domain where the quarks are deep inside the classically unaccesible region $R_{1,2}<R_d$. In this region one expects the relativistic effects, in particular the multi-quark components of the state, to play a significant role. The solution taking into account these effects is not yet available,[6] and the exact form of S_{res} is not known. However, even in the absence of the explicit solution, one can predict that the amplitude $S_{\mathrm{res}}(E)$, as the function of the total energy E of this state, must exhibit a resonance pole at the complex energy (3.16). If E is close to the resonance energy (given by the real part of (3.16)), this amplitude can be approximated by the Breit–Wigner formula

$$S_{\mathrm{res}}(E)\approx\frac{E/R-\Delta F+i\Gamma}{E/R-\Delta F-i\Gamma}, \tag{B.23}$$

where R is the spatial size of the system, and $\Delta F=E_{\mathrm{res}}/R\simeq 2\bar{\sigma}\,h+O(h^3)$ is the same as in (5.7). With this approximation for the "resonance scattering amplitude" $S_{\mathrm{res}}(E)$ in (B.21), and with the relativistic corrections described in BI taken into account, the wave function (B.21) can be written as

$$\psi(Y)=\mathrm{const}(F_A(Y-\epsilon')+\sigma_{\mathrm{res}}(\epsilon')\,F_B(Y-\epsilon')), \tag{B.24}$$

where

$$\sigma_{\mathrm{res}}(\epsilon')=-\frac{\Gamma(m,h)\,R}{mt^2\,\epsilon'}, \tag{B.25}$$

and F_A and F_B are the same perturbative solutions of (B.13) as in (B.16).

Now let us come back to the problem of the meson states, this time assuming a finite-size geometry of the system, with the spatial coordinate x compactified on a circle of finite circumference R. If h is sufficiently small, almost all the analysis of BI remains valid, with the exception of the bound-state condition (B.18), which has to be slightly modified. When the meson (i.e., the two-quark system with the confining interaction generated by the

---

[6] An attempt to apply the two-particle approximation in this region was made in an interesting recent paper.$^{(42)}$ We comment upon the result of this work at the end of Section 7.2.

magnetic field h) is put on a finite-size circle, its energy levels should be determined from some sort of periodicity condition imposed on the state wave function, rather then by (B.18). Again, unfortunately the two-quark approximation in general breaks down in the classically unaccessible domain $|X| \gg \epsilon$ (here $|X|$ is the rescaled quarks separation (B.9), and ϵ relates to the energy E as in (B.6)), where multi-quark components of the wave function become significant. Although the solution for the full wave function in this domain is not known, one can note that this problem is closely related to the above problem of determining the "scattering amplitude" S_{res} in (B.21), and the form (B.25) of the wave function still applies if one makes identifications

$$\epsilon' = \epsilon - mt\,(R - R_d), \qquad Y - \epsilon' = X - \epsilon, \tag{B.26}$$

which follow from the periodicity of the problem. With this, by demanding agreement between (B.16) and (B.24), one arrives at the equation

$$\sigma(\epsilon) = \sigma_{\mathrm{res}}(\epsilon - mt(R - R_d)), \tag{B.27}$$

which determines the R dependence of the finite-size energy levels $E_i(R) - E_0(R) = 2m + mt^2\epsilon_i(R)$ associated with the meson states; here $\epsilon_i(R)$ are the solutions of the Eq. (B.27).

Eq. (B.27) is derived within the two-quark approximation which is justified if h is small. It applies when R is sufficiently greater then R_d (otherwise the domain of validity of (B.24) does not exist). It is not difficult to see that in this domain (B.27) leads to a pattern of the finite-size energies very similar to what is shown in the Fig. 6a. Indeed, for small h the resonance width Γ is expected to be exponentially small (see Eq. (3.18)), and hence the function σ_{res} in the r.h.s. of (B.27) is very small everywhere exept when ϵ is close to its resonance pole $\epsilon_{\mathrm{res}}(R) \equiv mt(R - R_d)$. Therefore, Eq. (B.27) can hold either by virtue of ϵ being close to one of the zeroes of the function $\sigma(\epsilon)$, which leads to $E(R) - E_0(R)$ close to one of the meson masses M_i, or by virtue of ϵ being close to $\epsilon_{\mathrm{res}}(R)$, leading to $E(R) - E_0(R)$ close to ΔFR. When the both conditions are met, which happens when R approaches one of the "near-intersection" points $R_{i,i+1} = M_i/\Delta F$, one can use the linear approximation $\sigma(\epsilon) \simeq (\epsilon - \epsilon_i)\,\sigma'(\epsilon_i)$, which results in a quadratic equation for $\epsilon(R)$. This way one arrives at Eq. (5.13) for the separations $E_{i+1}(R) - E_i(R)$.

NOTE ADDED IN PROOF

The identification of the Yang–Lee critical point as the $c_{\mathrm{YL}} = -22/5$ minimal CFT, which we use in this paper, was extensively verified by numerical analysis of the Ising quantum chain in an interesting work.(59) Although the results in ref. 59 do not specifically concern the critical domain of the Ising chain and associated scaling functions, an estimate $\xi_0 = 0.19(1)$ for the position of the Yang–Lee singularity in the scaling function can be found there; it appears consistent with our result in Eq. (3.2).

ACKNOWLEDGMENTS

We are grafteful to Al. Zamolodchikov and S. Lukyanov for many discussions and suggestions at various stages of this work. P.F. would like to thank R. Roussev and E. Vitchev for helpful computational advices and also P. Zinn-Justin, V. Terras and C. Bolech for motivating conversations. A.Z. acknowledges helpful discussions with V. Kazakov, J. Lebowitz, A. Larkin and G. Falkovich. The work of P.F. was supported by the schollarship PRAXIS XXI BD 9102/96, from FCT, Portugal, and by a fellowship from *Calouste Gulbenkian Foundation*, Portugal. The work of A.Z. is supported by DOE Grant #DE-FG02-96ER10919.

REFERENCES

1. M. Caselle and M. Hasenbusch, Critical amplitudes and mass spectrum of the 2D Ising model in a magnetic field, *Nucl. Phys. B* **579**:667–703 (2000), (preprint `hep-th/9911216`).
2. M. Caselle, M. Hasenbusch, A. Pelissetto, and E. Vicari, *Irrelevant Operators in the Two-Dimensional Ising Model*, DFTT 17/2001, DESY 01-074, IFUP-TH 99/2001, Roma1-1963/01, June 2001 (preprint `cond-mat/0106372`).
3. M. Caselle, P. Grinza, and N. Magnoli, Correction induced by irrelevant operators in the correlators of the 2-d Ising model in a magnetic field, *J. Phys. A* **34**:8733–8750 (2001) (preprint `hep-th/0103263`).
4. L. Onsager, Crystal statistics. I. A two-dimensional model with an order-disorder transition, *Phys. Rev.* **65**:117–149 (1944).
5. B. Kaufman, Crystal statistics. II. Partition function evaluated by spinor analysis, *Phys. Rev.* **76**:1232–1243 (1949).
6. C. N. Yang, The spontaneous magnetization of a two-dimensional Ising model, *Phys. Rev.* **85**:808–816 (1952).
7. E. Barouch, B. M. McCoy, and T. T. Wu, Zero-field susceptibility of the two-dimensional Ising model near T_c, *Phys. Rev. Lett.* **31**:1409–1411 (1973).
8. T. T. Wu, B. M. McCoy, C. A. Tracy, and E. Barouch, Spin-spin correlation functions for the two-dimensional Ising model: Exact theory in the scaling region, *Phys. Rev. B* **13**:316–374 (1976).
9. A. B. Zamolodchikov, Integrals of motion and S-matrix of the (scaled) $T = T_c$ Ising model with magnetic field, *Int. J. Mod. Phys. A* **4**:4235–4248 (1989).
10. V. A. Fateev, The exact relations between the coupling constants and the masses of particles for the integrable perturbed conformal field theories, *Phys. Lett. B* **324**:45–51 (1994).
11. G. Delfino, Universal amplitude ratios in the two-dimensional Ising model, *Phys. Lett. B* **419**:291–295 (1998), (preprint `hep-th/9710019`).
12. J. W. Essam and D. L. Hunter, Classical behaviour of the Ising model above and below the critical temperature, *J. Phys. C* **1**:392–407 (1968).
13. S. Zinn, S.-N. Lai, and M. E. Fisher, Renormalized coupling constants and related amplitude ratios for Ising systems, *Phys. Rev. E* **54**:1176–1182 (1996).

14. M. Caselle, M. Hasenbusch, A. Pelissetto, and E. Vicari, High-precision estimate of g_4 in the 2D Ising model, *J. Phys. A* **33**:8171–8180 (2000), (preprint `hep-th/0003049`).
15. M. Caselle, M. Hasenbusch, A. Pelissetto, and E. Vicari, The critical equation of state of the 2D Ising model, *J. Phys. A* **34**:2923–2948 (2001), (preprint `cond-mat/0011305`).
16. V. P. Yurov and Al. B. Zamolodchikov, Truncated conformal space approach to scaling Lee–Yang model, *Int. J. Mod.Phys. A* **5**:3221–3245 (1990).
17. V. P. Yurov and Al. B. Zamolodchikov, Truncated-fermionic-space approach to the critical 2D Ising model with magnetic field, *Int. J. Mod. Phys. A* **6**:4557–4578 (1991).
18. C. N. Yang and T. D. Lee, Statistical theory of equations of state and phase transitions. I. Theory of condensation, *Phys. Rev.* **87**:404–409 (1952).
19. T. D. Lee and C. N. Yang, Statistical theory of equations of state and phase transitions. II. Lattice gas and Ising model, *Phys. Rev.* **87**:410–419 (1952).
20. J. S. Langer, Theory of the condensation point, *Ann. Phys.* **41**:108–157 (1967); *Ann. Phys.* **281**:941–990 (2000).
21. M. B. Voloshin, Decay of a metastable vacuum in (1+1) dimensions, *Yad. Fiz.* **42**:1017–1026 (1985); *Sov. J. Nucl. Phys.* **42**:644–649 (1985).
22. T. T. Wu and B. M. McCoy, *The Two-Dimensional Ising Model* (Harvard University Press, 1973).
23. G. Mussardo, Off-critical statistical models: factorized scattering theories and bootstrap program, *Phys. Rep.* **218**:215–379 (1992).
24. B. Berg, M. Karowski, and P. Weisz, Construction of Green's functions from an exact *S* matrix, *Phys. Rev. D* **19**:2477–2479 (1979).
25. L. P. Kadanoff and H. Ceva, Determination of an operator algebra for the two-dimensional Ising model, *Phys. Rev. B* **3**:3918–3939 (1971).
26. S. Sachdev, Universal, finite temperature, crossover functions of the quantum transition in the Ising chain in a transverse field, *Nucl. Phys. B* **464**:576–595 (1996), (preprint `cond-mat/9509147`).
27. A. I. Bugrij, *The Correlation Function in Two Dimensional Ising Model on the Finite Size Latice. I.* (preprint `hep-th/0011104`); *Form Factor Representation of the Correlation Function of the Two Dimensional Ising Model on a Cylinder* (preprint `hep-th/0107117`).
28. J. Balog, M. Niedermaier, F. Niedermayer, A. Patrascioiu, E. Seiler, and P. Weisz, The intrinsic coupling in integrable quantum field theories, *Nucl. Phys. B* **583**:614–670 (2000), (preprint `hep-th/0001097`).
29. M. E. Fisher, Yang–Lee edge singularitry and φ^3 field theory, *Phys. Rev. Lett.* **40**:1610–1613 (1978).
30. J. L. Cardy, Conformal invariance and the Yang–Lee edge singularity in two dimensions, *Phys. Rev. Lett.* **54**:1354–1356 (1985).
31. Al. B. Zamolodchikov, Thermodynamic Bethe ansatz in relativistic models: Scaling 3-state Potts and Lee–Yang models, *Nucl. Phys. B* **342**:695–720 (1990).
32. A. F. Andreev, Singularity of thermodynamic quantities at a first order phase transition point, *Sov. Phys. JETP* **18**:1415–1416 (1964).
33. M. E. Fisher, *University of Colorado, Boulder, Summer School Lectures, 1964* (University of Colorado Press, Boulder, 1965); *Proc. Centennial Conf. Phase Transformations* (Univ. Kentucky, 1965).
34. N. J. Günther, D. A. Nicole, and D. J. Wallace, Goldstone model in vacuum decay and first-order phase transitions, *J. Phys. A* **13**:1755–1767 (1980).
35. M. J. Lowe and D. J. Wallace, Instantons and the Ising model below T_c, *J. Phys. A* **13**:L381–L385 (1980).
36. C. K. Harris, The Ising model below T_c: calculation of non-universal amplitudes using a primitive droplet model, *J. Phys. A* **17**:L143–L419 (1984).

37. B. M. McCoy and T. T. Wu, Two-dimensional Ising model near T_c: Approximation for small magnetic field, *Phys. Rev. B* **18**:4886–4901 (1978).
38. J. S. Langer, Statistical theory of the decay of metastable states, *Annals Phys.* **54**:258–275 (1969).
39. I. Yu. Kobzarev, L. B. Okun, and M. B. Voloshin, Bubbles in metastable vacuum, *Yad. Fiz.* **20**:1229–1234 (1974); *Sov. J. Nucl. Phys.* **20**:644–646 (1975).
40. S. Coleman, Fate of the false vacuum: Semiclassical theory, *Phys. Rev. D* **15**:2929–2936 (1977).
41. C. G. Callan and S. Coleman, Fate of the false vacuum. II. First quantum corrections, *Phys. Rev. D* **16**:1762–1768 (1977).
42. S. B. Rutkevich, Decay of the metastable phase in $d = 1$ and $d = 2$ Ising models, *Phys. Rev. B* **60**:14525–14528 (1999), (preprint `cond-mat/9904059`).
43. V. Fateev, S. Lukyanov, A. Zamolodchikov, and Al. Zamolodchikov, Expectation values of local fields in Bullough–Dodd model and integrable perturbed conformal field theories, *Nucl. Phys. B* **516**:652–674 (1998), (preprint `hep-th/9709034`).
44. G. Delfino and G. Mussardo, The spin-spin correlation function in the two-dimensional Ising model in a magnetic field at $T = T_c$, *Nucl. Phys. B* **455**:724–758 (1995), (preprint `hep-th/9507010`).
45. J. L. Cardy and G. Mussardo, *S*-matrix of the Yang–Lee edge singularity in two dimensions, *Phys. Lett. B* **225**:275–278 (1989).
46. Al. B. Zamolodchikov, Thermodynamic Bethe ansatz for RSOS scattering theories, *Nucl. Phys. B* **358**:497–523 (1991).
47. Al. B. Zamolodchikov, Mass scale in the Sine-Gordon model and its reductions, *Int. J. Mod. Phys. A* **10**:1125–1150 (1995).
48. B. M. McCoy and T. T. Wu, Two-dimensional Ising field theory in a magnetic field: Breakup of the cut in the two-point function, *Phys. Rev. D* **18**:1259–1267 (1978).
49. G. Delfino, G. Mussardo, and P. Simonetti, Non-integrable quantum field theories as perturbations of certain integrable models, *Nucl. Phys. B* **473**:469–508 (1996), (preprint `hep-th/9603011`).
50. V. Privman and L. S. Shulman, Analytic continuation at first-order phase transitions, *J. Stat. Phys.* **29**:205–229 (1982).
51. J. S. Langer, Metastable states, *Physica* **73**:61–72 (1974).
52. J. Zinn-Justin, *Quantum Field Theory and Critical Phenomena* (Oxford University Press, 1989).
53. B. G. Nickel, On the singularity structure of the 2D Ising model susceptibility, *J. Phys. A* **32**:3889–3906 (1999); Addendum to "On the singularity structure of the 2D Ising model susceptibility," *J. Phys. A* **33**:1693–1711 (2000).
54. W. P. Orrick, B. G. Nickel, A. J. Guttmann, and J. H. H. Perk, Critical behaviour of the two-dimensional Ising susceptibility, *Phys. Rev. Lett.* **86**:4120–4123 (2001), (preprint `cond-mat/0009059`).
55. W. P. Orrick, B. G. Nickel, A. J. Guttmann, and J. H. H. Perk, The susceptibility of the square lattice Ising model: New developments, *J. Stat. Phys.* **102**:795–841 (2001), (preprint `cond-mat/0103074`).
56. P. Fonseca, S. Lukyanov, and A. Zamolodchikov, to be published.
57. A. LeClair, Spectrum generating affine Lie algebras in massive field theory, *Nucl. Phys. B* **415**:734–780 (1994), (preprint `hep-th/9305110`).
58. V. P. Yurov and Al. B. Zamolodchikov, Correlation functions of integrable 2D models of relativistic field theory; Ising model, *Int. J. Mod. Phys. A* **6**:3419–3440 (1991).
59. G. von Gehlen, Critical and off-critical conformal analysis of the Ising quantum chain in an imaginary field, *J. Phys. A* **24**:5371–5400 (1991).